Cell Reports

Article

Alterations of ceramide synthesis induce PD-L1 internalization and signaling to regulate tumor metastasis and immunotherapy response

Graphical abstract

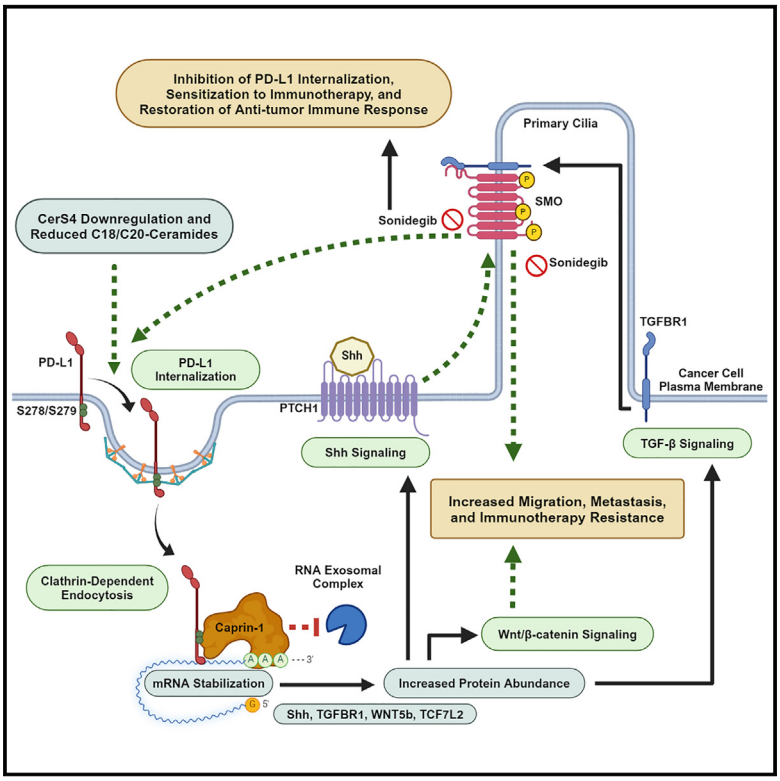

Highlights

- CerS4 knockdown drives migration/metastasis via Shh/TGF-β signaling and PD-L1 internalization
- The PD-L1/caprin-1 complex selectively stabilizes key mRNAs to promote migration/metastasis
- Targeting CerS4/PD-L1/caprin-1/Shh axis sensitized metastatic breast cancer to immunotherapy

Authors

Wyatt Wofford, Jisun Kim, Dosung Kim, ..., Shikhar Mehrotra, Ozgur Sahin, Besim Ogretmen

Correspondence

ogretmen@musc.edu

In brief

Wofford et al. show that CerS4 knockdown promotes PD-L1 internalization and signaling to enhance breast cancer migration/metastasis through Shh/TGF-β signaling. Targeting the CerS4/PD-L1/caprin-1/Shh axis sensitized metastatic breast cancer tumors to immunotherapy and impaired lung metastasis, offering a promising therapeutic strategy.

Wofford et al., 2024, Cell Reports *43*, 114532
August 27, 2024
https://doi.org/10.1016/j.celrep.2024.114532

CellPress

Cell Reports

CellPress
OPEN ACCESS

Article

Alterations of ceramide synthesis induce PD-L1 internalization and signaling to regulate tumor metastasis and immunotherapy response

Wyatt Wofford,[1,2] Jisun Kim,[1,2] Dosung Kim,[1,2] Alhaji H. Janneh,[1,2,6] Han Gyul Lee,[1,2] F. Cansu Atilgan,[1,2] Natalia Oleinik,[1,2] Mohamed Faisal Kassir,[1,2] Ozge Saatci,[1,2] Paramita Chakraborty,[1,2,3] Unal Metin Tokat,[5] Salih Gencer,[1,2,4] Breege Howley,[1,2] Philip Howe,[1,2] Shikhar Mehrotra,[1,2,3] Ozgur Sahin,[1,2] and Besim Ogretmen[1,2,7,*]

[1]Department of Biochemistry and Molecular Biology, Medical University of South Carolina, 86 Jonathan Lucas Street, Charleston, SC 29425, USA

[2]Hollings Cancer Center, Medical University of South Carolina, 86 Jonathan Lucas Street, Charleston, SC 29425, USA

[3]Department of Surgery, Medical University of South Carolina, 86 Jonathan Lucas Street, Charleston, SC 29425, USA

[4]Istanbul Medipol University, Health Science and Technologies Research Institute (SABİTA), Cancer Research Center, Istanbul, Turkey

[5]Department of Molecular Biology and Genetics, Bilkent University, Ankara, Turkey

[6]Present address: Cancer Biology and Genetics Program, Memorial Sloan Kettering Cancer Center, New York, NY 10065, USA

[7]Lead contact

*Correspondence: ogretmen@musc.edu

https://doi.org/10.1016/j.celrep.2024.114532

SUMMARY

Programmed death ligand 1, PD-L1 (CD274), facilitates immune evasion and exerts pro-survival functions in cancer cells. Here, we report a mechanism whereby internalization of PD-L1 in response to alterations of bioactive lipid/ceramide metabolism by ceramide synthase 4 (CerS4) induces sonic hedgehog (Shh) and transforming growth factor β receptor signaling to enhance tumor metastasis in triple-negative breast cancers (TNBCs), exhibiting immunotherapy resistance. Mechanistically, data showed that internalized PD-L1 interacts with an RNA-binding protein, caprin-1, to stabilize Shh/TGFBR1/Wnt mRNAs to induce β-catenin signaling and TNBC growth/metastasis, consistent with increased infiltration of $FoxP3^{+}$ regulatory T cells and resistance to immunotherapy. While mammary tumors developed in MMTV-PyMT/$CerS4^{-/-}$ were highly metastatic, targeting the Shh/PD-L1 axis using sonidegib and anti-PD-L1 antibody vastly decreased tumor growth and metastasis, consistent with the inhibition of PD-L1 internalization and Shh/Wnt signaling, restoring anti-tumor immune response. These data, validated in clinical samples and databases, provide a mechanism-based therapeutic strategy to improve immunotherapy responses in metastatic TNBCs.

INTRODUCTION

Metastasis is associated with increased cancer-related deaths.[1,2] Crosstalk between metabolic and oncogenic signaling in the regulation of tumor metastasis remains largely unknown. Transforming growth factor β (TGF-β) and Hedgehog (Shh) signaling, driven by sonic hedgehog (shh), regulate cancer cell proliferation, migration, and metastasis.[3–7] Shh signaling is kept inactive by the tumor suppressor Patched 1 (PTHC1) that binds and inhibits Smoothened (SMO), an oncogenic G-protein-coupled receptor (GPCR).[8,9] There are various TGF-β and Shh signaling inhibitors that can block solid tumor growth or metastasis with limited clinical efficacy.[10,11]

Immune checkpoint inhibitors have been efficacious in inducing anti-cancer immune functions.[12–14] Anti-PD-L1/PD-1 antibodies provide a robust anti-tumor response in patients with solid metastatic tumors.[15–17] PD-1 (programmed cell death 1) expressed on T cells binds programmed cell death ligand 1 (PD-L1) in cancer cells to prevent anti-tumor functions of T cells.[18] PD-L1 (CD274) is a transmembrane protein frequently upregulated in cancer cells to evade the host immune system.[19,20] In addition to its effects on the cell membrane to inhibit anti-tumor functions of T cells, PD-L1 exerts pro-survival functions by promoting inflammasome signaling, modulating TGF-β signaling, and influencing DNA-damage repair in cancer cells.[21–23] However, the mechanisms that regulate the intracellular pro-survival signaling activity of PD-L1 are understudied.

The plasma membrane provides a signaling platform to various serine/threonine kinase receptors, GPCRs, and transmembrane proteins, including TGFBR1/2, SMO, and PD-L1.[24–26] Sphingolipids play structural roles in regulating the rigidity and shape of the plasma membrane.[27,28] In addition, sphingolipids, especially ceramide, are crucial molecules with bioactive signaling roles.[29,30] Ceramide synthases generate *de novo* ceramides containing different fatty acyl chain lengths, which play distinct roles in membrane structure and signaling.[31,32] For example, CerS2-generated very-long-chain ceramides (C22/24-ceramide) induce cancer cell growth, while CerS4-generated long-chain ceramides

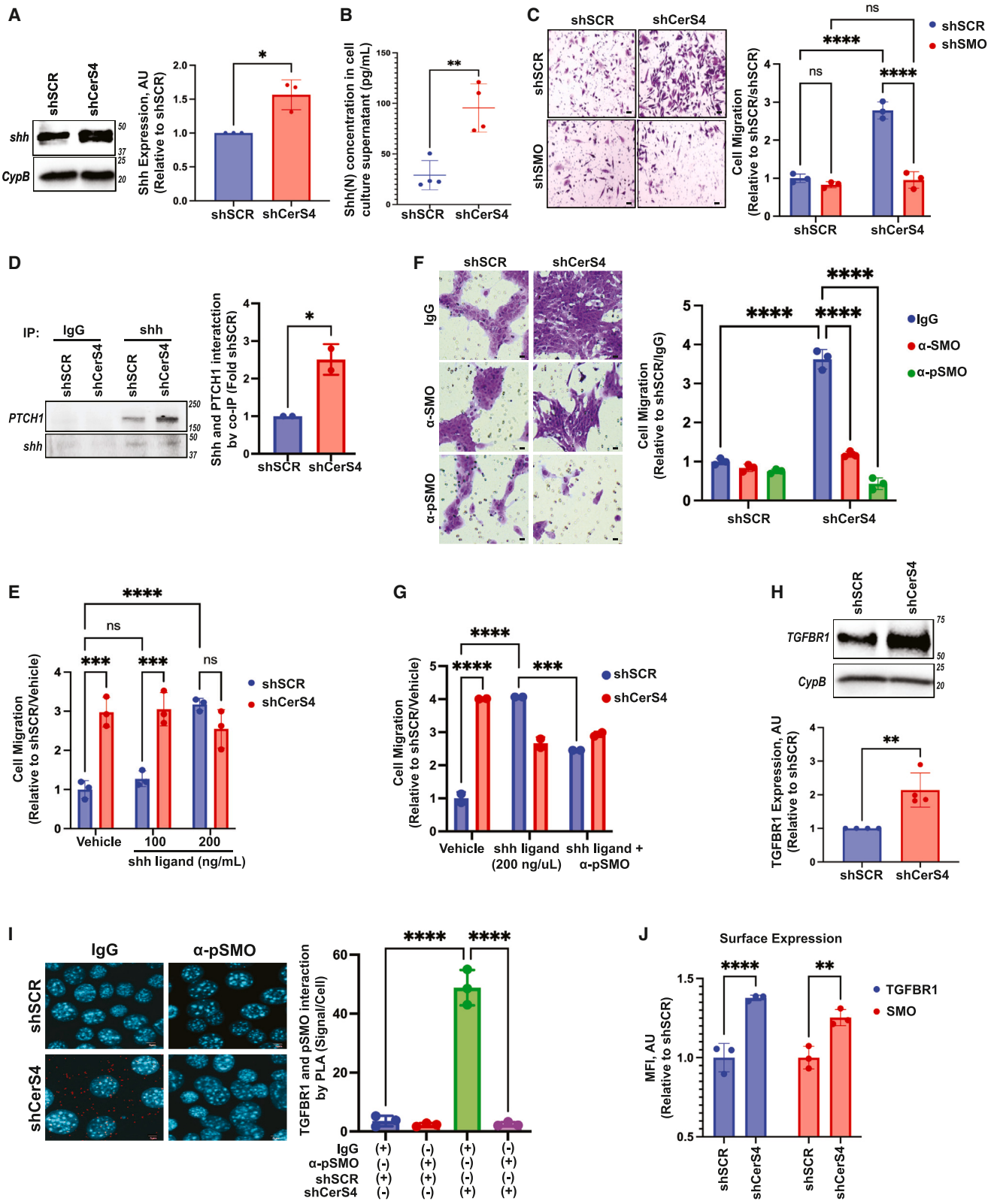

(legend on next page)

(C18/C20-ceramide) protect cancer cell migration/metastasis.[33,34] Our recent data showed that genetic loss or molecular knockdown of CerS4/C18-C20-ceramide enhances tumor metastasis in part via activation of the crosstalk between TGFBR1 and SMO signaling at the plasma membrane selectively activating the Shh pathway in primary cilia *in vitro* and *in vivo*.[34] However, possible involvement of intracellular PD-L1 signaling in this process remains unknown. Thus, in this work, we aimed to uncover the roles and mechanisms of reduced CerS4-generated ceramide synthesis in the regulation of PD-L1 internalization and its intracellular signaling to induce tumor metastasis and resistance to immunotherapy in triple-negative breast cancer (TNBC).

RESULTS

CerS4 knockdown activates Shh and TGFBR1 signaling to induce breast cancer cell migration

We examined the effects of short hairpin RNA (shRNA)-mediated knockdown of CerS4, CerS5, and CerS6 on the migration of 4T1 murine TNBC cells. Knockdown of CerS4 (>70%), which decreased C18:1-, C20-, and C20:1-ceramide generation (Figures S1A–S1C), enhanced the migration of 4T1 cells compared to SCR-shRNA-transfected controls (Figure S1D). shRNA-mediated knockdown of CerS5 or CerS6 did not significantly affect the migration of 4T1 cells (Figure S1D). Reconstitution of C18- and C20-ceramides using exogenous ceramides inhibited the migration of 4T1 cells transfected with CerS4-shRNAs compared to controls without affecting their growth (Figures S1E and S1F). These data demonstrate that downregulation of CerS4/C18-C20-ceramide induces cell migration, and reconstitution of ceramides prevents the migration of 4T1 cells.

CerS4/C18-C20-ceramide alterations induce cancer cell migration via Shh/SMO activation through TGF-β receptor 1/2 (TGFBR1/2) signaling.[34] Thus, we measured the effects of CerS4 knockdown on Shh protein expression and accumulation levels in 4T1 cells. Downregulation of CerS4 increased Shh expression and secretion into cell-culture media (compared to SCR-shRNA-transfected controls) (Figures 1A and 1B). shRNA-dependent knockdown of Shh almost completely prevented 4T1 cell migration (Figures S1G and S1H) in response to CerS4 knockdown. Also, downregulation of SMO by shRNA (Figure S1I) impaired the migration of 4T1 cells (Figure 1C). These data were also consistent with 2.5-fold increased association between Shh and PTCH1 in response to CerS4 knockdown compared to controls (Figure 1D), validating the activation of Shh/SMO signaling. Exogenous recombinant Shh ligand (200 ng/mL) increased migration without further impacting CerS4-knockdown-enhanced migration (Figure 1E). Inactivation of Shh/SMO signaling by our custom-developed antibody against the phosphorylated SMO protein (pSmo), developed using the peptide sequence EP(pS)ADVS(p)S(p)AWAQHVTC (S611/S615/S616) and by a commercially available SMO antibody that recognizes total SMO protein, inhibited 4T1 cell migration in CerS4-shRNA compared to SCR-shRNA transfected cells (Figure 1F).[35–37] Inhibition of Shh/SMO signaling by anti-pSMO antibody attenuated Shh ligand-mediated cell migration by 50% compared to controls (Figure 1G).

shRNA-mediated CerS4 knockdown enhanced the expression of TGFBR1 (100%) compared to SCR-shRNA-transfected controls (Figure 1H). Further, a proximity ligation assay (PLA) showed that pSMO is highly associated with TGFBR1 in 4T1 cells transfected with CerS4-shRNA compared to SCR-shRNA, consistent with the previously published findings (Figure 1I).[34] The anti-pSMO antibody exposure blocked this interaction between pSMO and TGFBR1 compared to immunoglobulin G (IgG)-exposed control cells (Figure 1I), suggesting the involvement of Shh and TGFBR1 crosstalk in the induction of 4T1 cell migration in response to alterations of CerS4/C18/20-ceramide metabolism. These data were supported by the inhibition of migration in response to exogenous Shh ligand (200 ng/mL) or CerS4 knockdown by pharmacologic inhibition of Shh/SMO using sonidegib or TGFBR1 using LY2157299 (galunisertib) compared to vehicle-treated controls (Figure S1J). Flow-cytometry data showed that the surface expression of SMO and TGFBR1 is higher in 4T1 cells transfected with CerS4-shRNA compared to SCR-shRNA (Figure 1J). These data reveal that downregulation of CerS4/C18/C20-ceramide induces the TGFBR1/Shh/pSMO signaling axis to enhance 4T1 cell migration, which is attenuated by Shh and TGFBR1 inhibition.

Figure 1. shRNA-mediated CerS4 knockdown activates Shh and TGFBR1 signaling

(A) Shh protein abundance in SCR or CerS4 shRNA-transfected 4T1 cells was detected in western blots. Data quantification is shown in right panel ($n = 3$).

(B) ELISA detected shh protein in the cell-culture supernatant from SCR or CerS4 shRNA-transfected 4T1 cells ($n = 4$).

(C) Representative images of migration assay measured in fibronectin-coated Boyden chambers ($n = 3$). Scale bars, 10 μm.

(D) Interaction of Shh and PTCH1 was detected by a co-immunoprecipitation with a Shh-targeting antibody and blotting for Shh and PTCH1 in 4T1 cells stably transfected with SCR or CerS4 shRNA ($n = 2$). Data quantification is shown in right panel.

(E) Effect of exogenous shh ligand (100–200 μg/mL) on cellular migration in 4T1 cells stably expressing SCR or CerS4 shRNA ($n = 3$).

(F) Effect of a neutralizing SMO and pSMO targeting antibody on cellular migration in 4T1 cells stably expressing SCR or CerS4 shRNA. Data quantification is shown in right panel ($n = 3$). Scale bars, 10 μm.

(G) Effect of exogenous shh ligand (200 μg/mL) on cellular migration in 4T1 cells stably expressing SCR or CerS4 shRNA with or without neutralizing pSMO antibody treatment ($n = 2$).

(H) TGFBR1 protein abundance in SCR or CerS4 shRNA-transfected 4T1 cells was detected by western blot. Data quantification is shown in lower panel ($n = 4$).

(I) Interaction of pSmo and TGFBR1 proteins was measured using a PLA in 4T1 cells stably expressing SCR or CerS4 shRNA with or without neutralizing pSMO antibody treatment. Data quantification is shown in right panel ($n = 3$). Scale bars, 5 μm.

(J) Cell-surface expression of SMO and TGFBR1 were determined using flow cytometry in 4T1 cells stably expressing SCR or CerS4 shRNA ($n = 3$).

Data represent means ± SD; Student's t test or two-way ANOVA was used to determine significance: $^{*}p < 0.05$, $^{**}p < 0.01$, $^{***}p < 0.001$, $^{****}p < 0.0001$; ns, not significant.

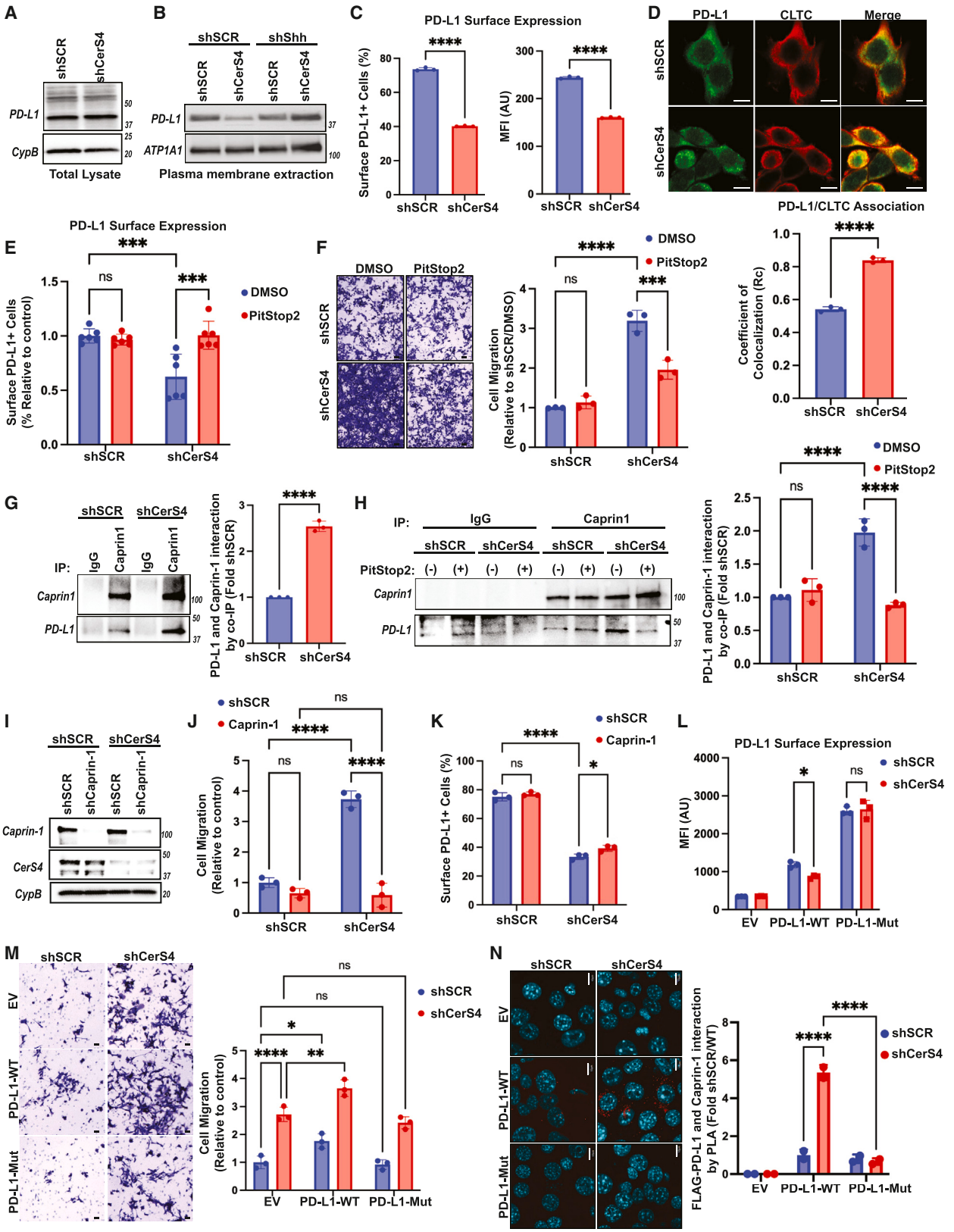

(legend on next page)

CerS4 knockdown results in the internalization of PD-L1 to enhance breast cancer cell migration

Because exogenous Shh or knockdown of CerS4 increased the expression of pSMO and TGFBR1, which are expressed on the plasma membrane, we sought to measure whether downregulation of CerS4 has any impact on other membrane proteins that impact cancer progression/metastasis, such as PD-L1.[38–40] The rationale to measure the effects of CerS4 knockdown on PD-L1 is due to clinical inefficiencies of immunotherapy in patients with TNBC.[41] Surprisingly, shRNA-dependent CerS4 knockdown resulted in a robust reduction of the plasma membrane localization of PD-L1, but not Na^+/K^+ ATPase (plasma membrane-localized control protein), without altering the overall cellular expression of PD-L1 compared to controls transfected with SCR-shRNAs (Figures 2A and 2B). Similar data were obtained by flow cytometry, whereby downregulation of CerS4 reduced plasma membrane localization of PD-L1 with or without interferon-γ (IFN-γ) exposure, which is known to stimulate PD-L1 expression, compared to SCR-shRNA-transfected 4T1 cells (Figures 2C and S2A). Gating strategies for flow-cytometry analyses are shown in Figure S2B. Because plasma membrane trafficking of PD-L1 is regulated by clathrin-dependent endocytosis, we measured the effects of CerS4 knockdown on PD-L1-clathrin heavy chain (CLTC) association.[42–44] Data showed that shRNA-mediated knockdown of CerS4 increased the localization between PD-L1 and CLTC (30%) (Figure 2D) while decreasing PD-L1 and E-cadherin co-localization (20%) (Figure S2C) compared to SCR-shRNA-transfected cells, suggesting increased internalization of PD-L1. Inhibition of clathrin-based endocytosis using PitStop2 restored plasma membrane expression of PD-L1 (Figure 2E) and inhibited cell migration (Figure 2F) in response to CerS4 knockdown. Moreover, shRNA-mediated knockdown of PD-L1 reduced the migration of 4T1 cells transfected with CerS4-shRNA compared to SCR-shRNA-transfected controls (50%) (Figure S2D), suggesting that internalized PD-L1 is involved in induced 4T1 cell migration in response to CerS4 knockdown. These data indicate that CerS4 knockdown induces PD-L1 internalization via a clathrin-dependent manner in 4T1 cells, which regulates enhanced cell migration signaling.

The intracellular PD-L1/caprin-1 complex mediates pro-migration signaling

To determine the mechanism by which intracellular PD-L1 signaling induces migration, we performed co-immunoprecipitation using an anti-PD-L1 antibody and identified proteins that interacted with PD-L1 by proteomics in 4T1 cells transfected with SCR-shRNA vs. CerS4-shRNA compared to IgG-associated proteins. These proteins were separated by PAGE and visualized by silver staining. We identified four distinct bands (#1, #3, #5, and #6) representing proteins that appeared to interact with PD-L1 in response to CerS4 knockdown compared to controls (Figure S2E). One of the top PD-L1-associated proteins responding to CerS4 knockdown was the RNA-binding protein caprin-1 (Figure S2F).[45,46] We validated the increased association of PD-L1 with caprin-1 in response to CerS4 knockdown in 4T1 cells compared to controls by co-immunoprecipitation and western blotting using anti-caprin-1 and anti-PD-L1 antibodies (Figure 2G, lower bands). CerS4 knockdown did not have any detectable effect on the caprin-1 protein levels compared to controls (Figure 2G, upper bands). Inhibition of PD-L1 internalization by PitStop2 almost completely abrogated PD-L1/caprin-1 interaction in response to CerS4 knockdown

Figure 2. CerS4 knockdown results in the internalization of PD-L1 to enhance breast cancer cell migration

(A) PD-L1 protein abundance in SCR or CerS4 shRNA-transfected 4T1 cells was detected in western blots ($n = 2$).

(B) Plasma membrane proteins were isolated from 4T1 cells stably expressing SCR or CerS4 shRNA, and PD-L1 abundance was detected by western blotting. Na^+/K^+ ATPase (ATP1A1) was a loading control for the plasma membrane fraction ($n = 2$).

(C) Cell-surface expression of PD-L1 (percentage of positive cells and mean fluorescent intensity) was determined by flow cytometry in 4T1 cells stably expressing SCR or CerS4 shRNA after treatment with 100 μg/mL IFN-γ for 48 h ($n = 3$).

(D) Immunofluorescence was performed in 4T1 cells stably expressing SCR or CerS4 shRNA using anti-PD-L1 and anti-clathrin heavy chain (CLTC) antibodies ($n = 3$). Data quantification is shown in lower panel. Scale bars, 10 μm.

(E) Cell-surface expression of PD-L1 was determined by flow cytometry in 4T1 cells stably expressing SCR or CerS4 shRNA with or without treatment with PitStop2 (30 μM for 1 h) ($n = 6$).

(F) Effect of PitStop2 (5 μM for 24 h) on cellular migration in 4T1 cells stably expressing SCR or CerS4 shRNA. Data quantification is shown in right panel ($n = 3$). Scale bars, 10 μm.

(G) Interaction of PD-L1 and caprin-1 was detected by co-immunoprecipitation and western blotting in 4T1 cells stably transfected with SCR or CerS4 shRNAs. Data quantification is shown in right panel ($n = 3$).

(H) Effect of PitStop2 treatment (30 μM for 1 h) on PD-L1 and caprin-1 in 4T1 cells stably expressing SCR or CerS4 shRNA was determined by co-immunoprecipitation ($n = 3$). Data quantification is shown in right panel.

(I) Caprin-1 and CerS4 protein abundance in 4T1 cells stably expressing either SCR or caprin-1 shRNA in the presence of SCR or CerS4 shRNA was detected by western blotting ($n = 3$).

(J) Effect of caprin-1 expression on the cellular migration of 4T1 cells stably transfected with SCR and CerS4 shRNA or SCR and caprin-1 shRNA was determined ($n = 3$).

(K) Cell-surface expression of PD-L1 was determined by flow cytometry in 4T1 cells stably expressing SCR or CerS4 shRNA and SCR or caprin-1 shRNA ($n = 3$).

(L) Cell-surface expression of WT-PD-L1-FLAG vs. Mut-PD-L1-FLAG was determined by flow cytometry in 4T1 cells stably expressing SCR or CerS4 shRNA ($n = 3$).

(M) The effect of WT-PD-L1-FLAG vs. Mut-PD-L1-FLAG on the cellular migration of 4T1 cells stably transfected with SCR and CerS4 shRNAs was determined. Data quantification is shown in right panel ($n = 3$). Scale bars, 10 μm.

(N) Interaction between WT-PD-L1-FLAG vs. Mut-PD-L1-FLAG (with S278A/S279A conversions) and caprin-1 using a PLA assay in 4T1 cells stably transfected with SCR and CerS4 shRNAs using anti-FLAG and anti-caprin-1 antibodies. Data quantification is shown in right panel ($n = 2$). Scale bars, 10 μm.

Data represent means ± SD; Student's t test or two-way ANOVA was used to determine significance: $^*p < 0.05$, $^{**}p < 0.01$, $^{***}p < 0.001$, $^{****}p < 0.0001$; ns, not significant.

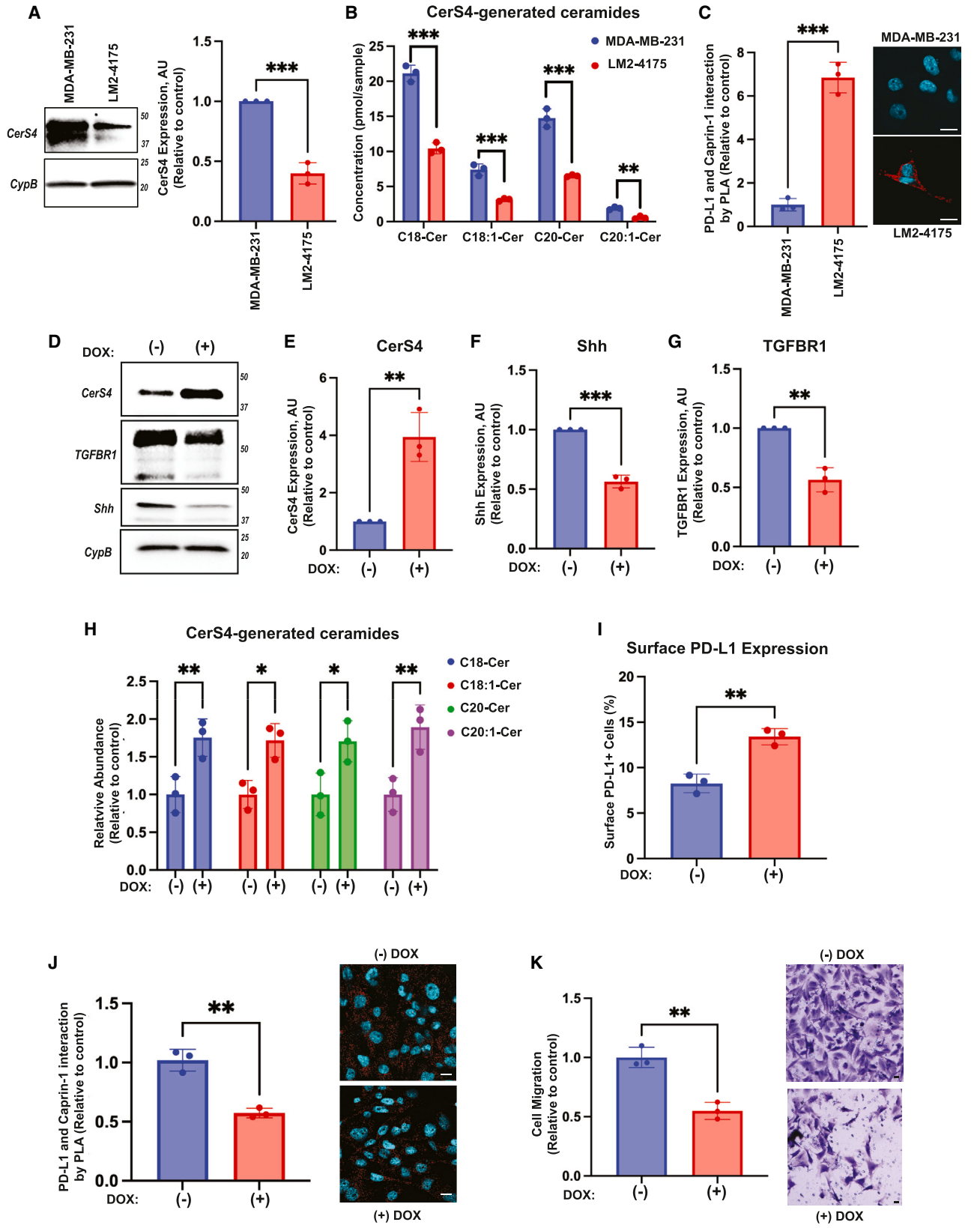

(legend on next page)

(Figure 2H). Increased PD-L1/caprin-1 association in response to CerS4 knockdown (2-fold), which increased migration (50%), was also validated in human MDA-MB-231 breast cancer cells (Figures S2F–S2H).

To determine the role of caprin-1 in PD-L1's intracellular signaling, we knocked down caprin-1 expression using shRNA (Figure 2I). Caprin-1 knockdown attenuated 4T1 cell migration in response to CerS4 knockdown compared to SCR-shRNA-transfected controls without preventing PD-L1 internalization (Figures 2J and 2K). Caprin-1 knockdown reduced interaction between Shh/PTCH1 by PLA in CerS4-shRNA-transfected cells compared to controls (Figure S2I).

To define whether the PD-L1/caprin-1 complex induces cell migration, we transfected SCR and CerS4 shRNA-expressing 4T1 cells with expression plasmids encoding wild-type (WT) or mutant PD-L1 with S278A and S279A conversions that are within the intracellular domain of PD-L1 which might be involved in protein-protein interaction (Figure S2J). Surface expression of the WT and mutant PD-L1 proteins was validated, and mutant PD-L1 had significantly higher surface expression (2-fold) despite similar overall cellular levels (Figure 2L). Ectopic expression of WT-PD-L1, but not mutant PD-L1 (S278A/S279A), increased migration of SCR-shRNA-transfected cells (50%) compared to empty vector (EV)-transfected controls (Figure 2M). Moreover, while WT-PD-L1 further increased cell migration (50%), mutant PD-L1 (S278A/S279A) had no impact in this process in response to CerS4 knockdown (Figure 2M). WT-PD-L1 was found to interact with caprin-1 while mutant PD-L1 did not (Figure 2N). These data suggest that caprin-1 is not involved in the S278/S279-dependent internalization process of PD-L1 but is critical for internalized PD-L1 signaling in response to CerS4 knockdown to induce cell migration.

Ectopic expression of CerS4 restores C18/C20-ceramide generation and prevents PD-L1/caprin-1 interaction

To determine whether the downregulation of CerS4, without any molecular manipulation, is associated with human metastatic breast cancer cells, we measured its expression in human MDA-MB-231 compared to its isogenic metastatic counterpart LM2-4175 cells. CerS4 protein expression was found to be downregulated (60%) in metastatic LM2-4175 compared to MDA-MB-231 cells (Figure 3A). Lower CerS4 expression in LM2-4175 cells was also consistent with decreased C18/C20-ceramides (50%), 7-fold increase in PD-L1/caprin-1 interaction (Figures 3B and 3C), and enhanced Shh abundance (20%) (Figure S3A) compared to MDA-MB-231 cells. These data suggest that downregulation of CerS4/C18/C20-ceramide synthesis induces PD-L1/caprin-1 interaction in metastatic LM2-4175 human breast cancer cells.

We then measured the roles of restoring CerS4/C18/C20-ceramide metabolism in regulating TGFBR1/Shh signaling and PD-L1 internalization in LM2-4175 cells. Doxycycline (Dox^+)-induced CerS4 (4-fold) enhanced C18/C20-ceramide accumulation (50%) and resulted in the reduction of TGFBR1 and Shh expression (50%) compared to uninduced (Dox^-) controls (Figures 3D–3H). Induction of CerS4/C18/C20-ceramide (Dox^+) also restored the expression of PD-L1 on the plasma membrane (Figure 3I) and prevented PD-L1 internalization (decreasing PD-L1/caprin-1 association) (Figure 3J). Moreover, Dox-induced CerS4 expression abrogated the migration compared to controls (Dox^-) in LM2-4175 cells (Figure 3K). These data demonstrate that while CerS4-C18/C20-ceramide metabolism is altered in metastatic LM2-4175 breast cancer cells, reconstitution of CerS4-C18/C20-ceramide reduced TGFBR1/Shh abundance, prevented PD-L1 internalization, and inhibited cell migration.

The PD-L1/caprin-1 complex stabilizes Shh and TGFBR1 mRNAs to induce cell migration

Because caprin-1, an RNA-binding protein, also induces stress granules, we measured the effects of CerS4 knockdown on the co-localization of caprin-1 or PD-L1 with a stress-granule marker, poly(A) binding protein (PABP), using immunofluorescence compared to SCR-shRNA transfections.[47,48] Data showed that CerS4 knockdown did not greatly affect caprin-1/PABP or PD-L1/PABP co-localization compared to controls (Figures S3B and S3C), suggesting that stress-granule formation by caprin-1 might be dispensable for the pro-migratory signaling roles of the PD-L1/caprin-1 complex.

We also tested whether internalized WT-PD-L1, which associates with caprin-1 and not the mutant (S278A/S279A)-PD-L1, induces caprin-1 interaction with Shh and TGFBR1 mRNAs, since PD-L1 was shown to directly interact with and stabilize mRNAs, including Shh and TGFBR1.[22,23] Thus, we performed RNA

Figure 3. Ectopic expression of CerS4 restores C18/C20-ceramide generation and surface PD-L1 accumulation

(A) CerS4 protein abundance in MDA-MB-231 and LM2-4175 cells was detected by western blotting. Data quantification is shown in right panel ($n = 3$).

(B) The abundance of CerS4-generated ceramides in MDA-MB-231 and LM2-4175 cells was determined using LC-MS/MS-based lipidomics analysis ($n = 3$).

(C) Interaction between PD-L1 and caprin-1 was detected by PLA using anti-PD-L1 and anti-caprin-1 antibodies in MDA-MB-231 and LM2-4175 cells. Data quantification is shown in left panel ($n = 3$). Scale bars, 20 μm.

(D–G) CerS4 (D and E), Shh (F), and TGFBR1 (G) abundance was determined in doxycycline-inducible CerS4 expression LM2-4175 cells after 48 h in 5 μg/mL doxycycline detected by western blotting using an anti-CerS4, anti-TGFBR1, and anti-Shh antibodies. Data quantification is shown in right panels ($n = 3$).

(H) The abundance of CerS4-generated ceramides in doxycycline-inducible CerS4 expression LM2-4175 cells was determined using LC-MS/MS-based lipidomics analysis. The raw values were normalized to the control conditions for each ceramide species ($n = 3$).

(I) Cell-surface expression of PD-L1 was determined by flow cytometry in doxycycline-inducible CerS4 expression LM2-4175 cells after 48 h in 5 μg/mL doxycycline ($n = 3$).

(J) Interaction between PD-L1 and caprin-1 was detected by PLA using anti-PD-L1 and anti-caprin-1 antibodies in doxycycline-inducible CerS4 expression LM2-4175 cells after 48 h in 5 μg/mL doxycycline. Data quantification is shown in left panel ($n = 3$). Scale bars, 20 μm.

(K) Cellular migration was measured in doxycycline-inducible CerS4 expression LM2-4175 cells after 48 h in 5 μg/mL doxycycline. Data quantification is shown in left panel ($n = 3$). Scale bars, 10 μm.

Data represent means ± SD; Student's t test was used to determine significance: $^*p < 0.05$, $^{**}p < 0.01$, $^{***}p < 0.001$, $^{****}p < 0.0001$; ns, not significant.

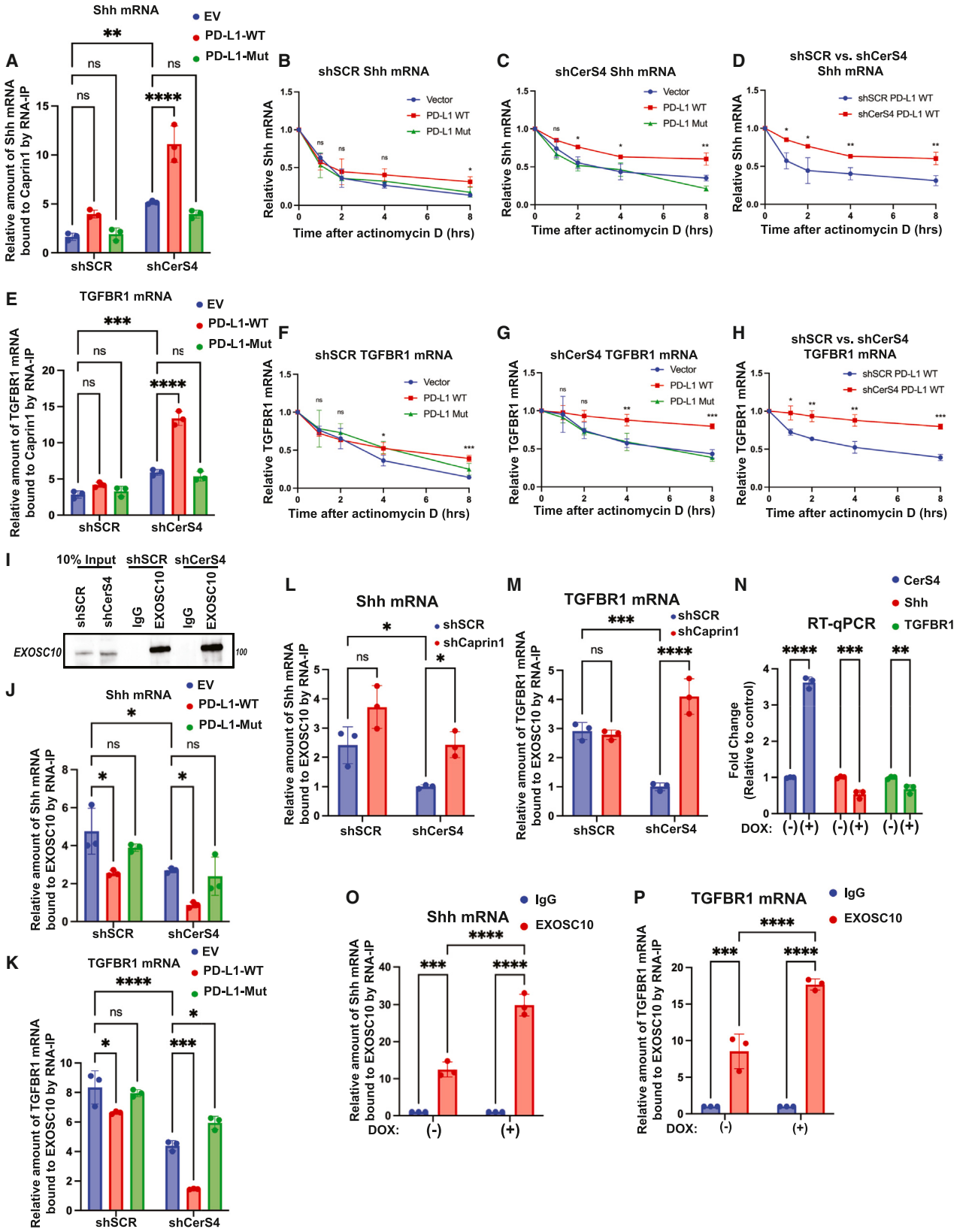

(legend on next page)

immunoprecipitation (RNA-IP) to measure the binding of caprin-1 with Shh mRNA and TGFBR1 mRNA and measure their stability in the absence/presence of actinomycin D for 0-, 2-, 4-, 6-, and 8-h treatments in 4T1 cells stably expressing SCR vs. CerS4 shRNAs transfected with EV, WT-PD-L1, or mutant (S278A/S279A)-PD-L1. WT-PD-L1, but not the mutant PD-L1, enhanced the binding of caprin-1 with Shh (2-fold) and TGFBR1 (2.5-fold) in CerS4-shRNA-expressing cells, increasing their mRNA half-lives from 4 h to >8 h compared to SCR-shRNA-expressing controls (Figures 4A–4H, respectively).

We then measured the association of their mRNAs with an exoenzyme, exosome component 10 (EXOSC10), using RNA-IPs. EXOSC10, which binds and degrades mRNAs, was shown to compete with PD-L1 for access to mRNAs for degradation.[23] Expression of WT-PD-L1, which associates with caprin-1, and not the mutant (S278A/S279A)-PD-L1, vastly decreased the binding of EXOSC10 (equal EXOSC10 pull-downs were validated, Figure 4I) with Shh and TGFBR1 mRNAs in both SCR and CerS4-shRNA-expressing 4T1 cells (Figures 4J and 4K). Knockdown of caprin-1 increased the association of Shh or TGFBR1 mRNAs with EXOSC10 (2.5- or 2.0-fold) in response to CerS4 knockdown (Figures 4L and 4M).

Also, we measured the effects of ectopic expression of CerS4 on the binding of EXOSC10 to Shh and TGFBR1 mRNA and their mRNA abundance in metastatic LM2-4175 cells by RNA-IPs. Dox-induced (Dox^+) expression of CerS4 (3.5-fold) reduced mRNA abundance of Shh and TGFBR1 (Figure 4N), consistent with the increased association of Shh and TGFBR1 mRNAs with EXOSC10 (3- and 2-fold, respectively) compared to uninduced (Dox^-) cells (Figures 4O and 4P). These data reveal that internalized PD-L1 binds caprin-1, inducing its binding to Shh and TGFBR1 mRNAs to stabilize their half-lives by reducing their degradation by RNA-degrading exoenzyme EXOSC10 in response to altered CerS4/C18/C20-ceramide synthesis.

The PD-L1/caprin-1 complex induces Wnt/β-catenin signaling in response to CerS4 knockdown

We then identified additional downstream mediators of the PD-L1/caprin-1 complex and TGFBR1/Shh signaling that regulate cell migration by RNA-IP using anti-caprin-1 in 4T1 cells stably transfected with SCR or CerS4 shRNAs or anti-EXOSC10 in Dox-inducible CerS4 LM2-4175 cells. We used global RNA sequencing using mRNAs bound to caprin-1 or EXOSC10 compared to IgG-bound mRNAs as controls. Data showed that mRNA interaction with caprin-1 and EXOSC10 in response to CerS4 modulation might regulate a diverse array of mRNAs whose encoded proteins are known to play roles in critical pathways, including amino acid biosynthesis, angiogenesis, Ras signaling, oxidative phosphorylation, and Wnt signaling (Figures S4A–S4C). These data revealed that caprin-1 and EXOSC10 are associated with many mRNAs involved in the stimulation of Wnt signaling, including Wnt7a, Wnt7b, and Wnt5b (Figure S4D). We also noticed that caprin-1 and EXOSC10 were associated with regulatory factors for Wnt signaling, such as TFC7L2 and Tle4 mRNA (Figure S4D), both known downstream regulators of Wnt/β-catenin signaling, which regulates cancer growth and metastasis. We then performed additional RNA-IP and qPCR experiments, which validated increased caprin-1 binding with TCF7L2 and Wnt5b mRNA in response to CerS4 knockdown in 4T1 cells (Figures S4E and S4F). These data were also consistent with a 3.5-fold and 2-fold increase in TCF7L2 and Wnt5b protein abundance in 4T1 cells in which CerS4 is stably knocked down compared to SCR-shRNA-transfected controls, respectively (Figure S4G). These data suggest that caprin-1 might induce Wnt/β-catenin signaling by binding to TCF7L2 mRNA and Wnt5b mRNA in response to CerS4 knockdown, possibly through the PD-L1/caprin-1 complex. While inhibition of Shh using sonidegib prevented PD-L1/caprin-1 association, Wnt/β-catenin inhibitor E7386 (lenvatinib) had no detectable impact on PD-L1/caprin-1 interaction in response to CerS4 knockdown (Figure S4H), supporting that the PD-L1/caprin-1 complex might be an upstream regulator of the Wnt/β-catenin signaling when CerS4/C18/C20-ceramide metabolism is altered. Inhibition of Wnt/β-catenin by E7386 or tegatrabetan largely inhibited the migration of 4T1 cells in response to CerS4 knockdown compared to SCR-shRNA-transfected controls (Figure S4I). These data suggest that while there is a crosstalk between the PD-L1/caprin-1 complex and

Figure 4. The PD-L1/caprin-1 complex stabilizes Shh and TGFBR1 mRNAs to induce cell migration

(A) Interaction between caprin-1 and Shh mRNA was quantified using RNA-immunoprecipitation coupled RT-qPCR in 4T1 cells stably expressing SCR or CerS4 shRNA with empty vector, WT-PD-L1-FLAG, or Mut-PD-L1-FLAG overexpressed ($n = 3$).

(B–D) Stability of Shh mRNA was determined in 4T1 cells stably expressing SCR or CerS4 shRNA with empty vector, WT-PD-L1-FLAG, or Mut-PD-L1-FLAG overexpressed along with actinomycin D (5 μg/mL) treatment ($n = 3$).

(E) Interaction between caprin-1 and TGFBR1 mRNA was quantified using RNA-immunoprecipitation coupled RT-qPCR with an anti-caprin-1 antibody in 4T1 cells stably expressing SCR or CerS4 shRNA with empty vector, WT-PD-L1-FLAG, or Mut-PD-L1-FLAG overexpressed ($n = 3$).

(F–H) Stability of TGFBR1 mRNA was determined in 4T1 cells stably expressing SCR or CerS4 shRNA with empty vector, WT-PD-L1-FLAG, or Mut-PD-L1-FLAG overexpressed along with actinomycin D (5 μg/mL) treatment ($n = 3$).

(I) Abundance and immunoprecipitation of EXOSC10 were determined by western blotting in 4T1 cells stably expressing SCR or CerS4 shRNA ($n = 2$).

(J and K) Interaction between EXOSC10 and Shh (J) or TGFBR1 (K) mRNA was quantified using RNA-immunoprecipitation coupled RT-qPCR with an anti-EXOSC10 antibody in 4T1 cells stably expressing SCR or CerS4 shRNA with empty vector, WT-PD-L1-FLAG, or Mut-PD-L1-FLAG overexpressed ($n = 3$).

(L and M) The interaction between EXOSC10 and Shh (L) or TGFBR1 (M) mRNA was quantified using RNA-immunoprecipitation coupled RT-qPCR with an anti-EXOSC10 antibody in 4T1 cells stably expressing SCR or CerS4 shRNA and SCR or caprin-1 shRNA ($n = 3$).

(N) Expression of CerS4, Shh, and TGFBR1 was determined by RT-qPCR in doxycycline-inducible CerS4 expression LM2-4175 cells after 48 h in 5 μg/mL doxycycline ($n = 3$).

(O and P) The interaction between EXOSC10 and Shh (O) or TGFBR1 (P) mRNA was quantified using RNA-immunoprecipitation coupled RT-qPCR with an anti-EXOSC10 antibody in doxycycline-inducible CerS4 expression LM2-4175 cells after 48 h in 5 μg/mL doxycycline ($n = 3$).

Data represent means ± SD; one-way or two-way ANOVA was used to determine significance: $^*p < 0.05$, $^{**}p < 0.01$, $^{***}p < 0.001$, $^{****}p < 0.0001$; ns, not significant.

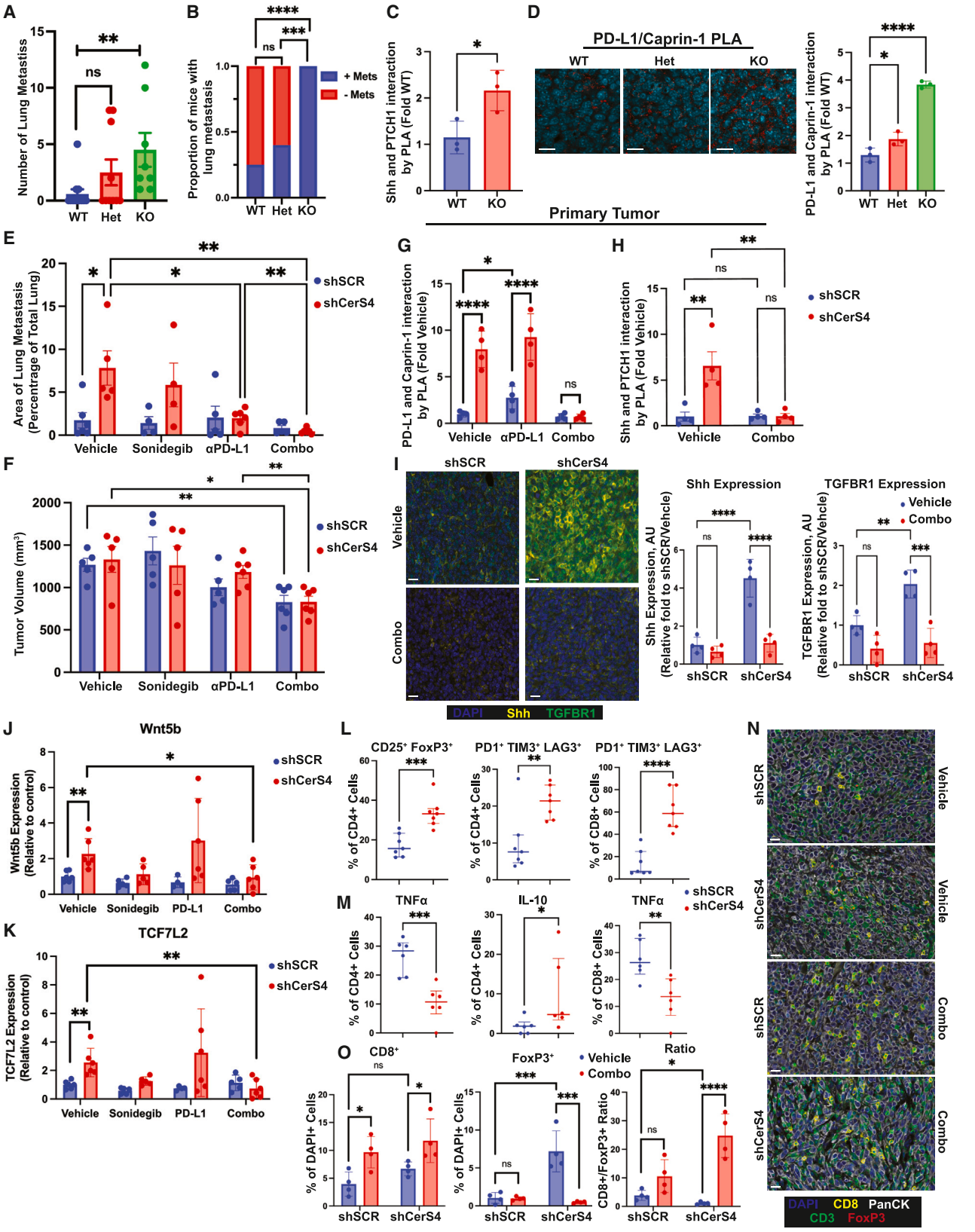

(legend on next page)

TGFBR1/Shh signaling, the PD-L1/caprin-1 interaction plays an upstream regulatory role to induce Wnt/β-catenin signaling in response to reduced CerS4-generated C18/C20-ceramide synthesis.

Genetic loss of CerS4 enhances lung metastasis of MMTV-PyMT-induced mammary tumors

To determine whether alterations of CerS4 play a role in inducing breast tumor metastasis *in vivo*, we crossbred mouse mammary tumor virus MMTV-PyMT with CerS4 knockouts (KOs) to generate MMTV-PyMT/CerS4$^{+/-}$ (Het) and MMTV-PyMT/CerS4$^{-/-}$ (KO) mice (Figure S5A). The data showed that while 25% (3 of 12) of the MMTV-PyMT/CerS4$^{+/+}$ (WT) control mice (5 months old) exhibited lung metastasis, MMTV-PyMT/CerS4$^{+/-}$ (5 months old) and MMTV-PyMT/CerS4$^{-/-}$ mice (5 months old) had 40% (4 of 10) and 100% (8 of 8) lung metastasis, respectively (Figures 5A and 5B). There were no differences in the growth of primary breast tumors in MMTV-PyMT/CerS4$^{+/-}$ and MMTV-PyMT/CerS4$^{-/-}$ compared to MMTV-PyMT/CerS4$^{+/+}$ controls (Figure S5B). After the growth/metastasis measurements were completed, we measured Shh activation by measuring Shh/PTCH1 interaction and PD-L1 internalization by measuring PD-L1/caprin-1 interaction by PLA in metastatic breast tumors isolated from the lungs of the mice shown in Figures 5A and S5A. Shh/PTCH1 association was increased 2-fold in CerS4$^{-/-}$ (KO) compared to CerS4$^{+/+}$ (WT) tumors (Figure 5C). Also, PD-L1/caprin-1 interaction was enhanced 1.8- and 3.9-fold in tumors obtained from CerS4$^{+/-}$ (Het) and CerS4$^{-/-}$ (KO) compared to CerS4$^{+/+}$ (WT) tumors, respectively (Figure 5D). These data suggest that genetic loss of CerS4 results in enhanced lung metastasis of MMTV-PyMT-mediated breast tumors concomitant with the Shh/SMO activation and internalization of PD-L1, forming the PD-L1/caprin-1 complex *in vivo*.

We then measured immune cell populations in primary breast tumors and metastatic lung tissues isolated from MMTV-PyMT/CerS4$^{+/+}$ (WT) and MMTV-PyMT/CerS4$^{-/-}$ (KO) mice by multiplexed immunofluorescence using antibodies that recognize CD4, CD8, or FoxP3 (pan-cytokeratin [PanCK] staining was used to identify tumor lesions). There was a slight increase in the abundance of CD8$^+$ and CD4$^+$/FoxP3$^+$ T cell populations in the primary breast tumor tissues obtained from CerS4$^{-/-}$ (KO) compared to control mice (CerS4$^{+/+}$ WT) (Figure S5C). However, in metastatic lung tumor tissues, there was a significant increase in the abundance of CD4$^+$/Fox3P$^+$ regulatory T cells (Tregs) isolated from CerS4$^{-/-}$ (KO) compared to control mice (CerS4$^{+/+}$ WT) (Figure S5C). These data indicate that genetic loss of CerS4 might mediate immune suppression via, at least in part, increased abundance of Fox3P$^+$ Tregs in metastatic breast tumors *in vivo*, consistent with PD-L1 internalization and caprin-1 interaction.

Inhibition of Shh and PD-L1 attenuates 4T1-derived mammary tumor growth and metastasis *in vivo*

Because genetic loss of CerS4 in metastatic mammary tumors suggested immune suppression concomitant with Shh activation and PD-L1 internalization, we hypothesized that inhibition of Shh and PD-L1 using sonidegib and anti-PD-L1 antibody alone or in combination might limit breast tumor growth and metastasis *in vivo*. To test this hypothesis, we implanted 4T1 cells stably transfected with SCR or CerS4 shRNAs into the mammary fat pads of Balb/c mice. After primary tumors became palpable, we treated the mice with vehicle, sonidegib, anti-PD-L1 antibody, or sonidegib + anti-PD-L1 antibody in combination (Combo) and measured its effects on tumor size and lung metastasis. CerS4 knockdown increased lung metastasis compared to vehicle-treated and shSCR-transfected tumors (Figures 5E and S5D). Treatment of these mice with anti-PD-L1 antibody or combination of sonidegib + anti-PD-L1 (Combo) inhibited lung metastasis of shCerS4 tumors compared to vehicle- or sonidegib-treated controls (Figure 5E). CerS4 knockdown did not affect primary tumor growth compared to shSCR tumors. Only the

Figure 5. The CerS4/PD-L1/caprin-1 axis drives TNBC metastasis and is sensitive to pharmacological inhibition

(A–D) Primary mammary tumors and lungs were collected from MMTV-PyMT-CerS4$^{+/+}$, -CerS4$^{+/-}$, and -CerS4$^{-/-}$ mice after 150 days. (A) The number of metastatic lung nodules from MMTV-PyMT-CerS4$^{+/+}$ (n = 12), -CerS4$^{+/-}$ (n = 10), and -CerS4$^{-/-}$ (n = 8) mice were quantified by an independent pathologist after H&E staining of lungs collected after 150 days. (B) The percentage of mice that developed lung metastasis was calculated. (C) Interaction between shh and PTCH1 was detected by PLA assay using anti-Shh and anti-PTCH1 antibodies in metastatic lung nodules from MMTV-PyMT-CerS4$^{+/+}$ and MMTV-PyMT-CerS4$^{-/-}$ mice (n = 3). (D) Interaction between PD-L1 and caprin-1 was detected by PLA assay using anti-PD-L1 and anti-caprin-1 antibodies in metastatic lung nodules from MMTV-PyMT-CerS4$^{+/+}$ and MMTV-PyMT-CerS4$^{-/-}$ mice. Quantification of data is shown in the left panel (n = 3). Scale bars, 10 μm.

(E–O) 4T1-derived tumors stably expressing SCR or CerS4 shRNA were established in BALB/c mice unilaterally. After 1 week, the mice were treated with vehicle (n = 6 SCR and n = 5 CerS4), sonidegib (n = 4 SCR and n = 4 CerS4), anti-PD-L1 therapy (n = 5 SCR and n = 6 CerS4), or a combination (n = 5 SCR and n = 6 CerS4) for 21 days. (E) The total area of lung metastasis was determined using Akoya Inform analysis software. (F) Endpoint primary tumors were collected and weighed. (G and H) The interaction between PD-L1 and caprin-1 (G) and Shh and PTCH1 (H) was detected by PLA assay using anti-PD-L1 and anti-caprin-1 or anti-Shh and anti-PTCH-1 antibodies, respectively, in primary tumors from the vehicle, anti-PD-L1, or combination groups (n = 4). (I) The expression of Shh and TGFBR1 in primary tumors from the vehicle or combination groups was determined by multiplexed immunofluorescence using anti-Shh and anti-TGFBR1 antibodies. Data quantification is shown in right panels (n = 4). Scale bars, 20 μm. (J and K) The expression of Wnt5b (J) and TCF7L2 (K) in primary tumors was determined by RT-qPCR on tumors from vehicle (n = 6 SCR and n = 6 CerS4), sonidegib (n = 5 SCR and n = 5 CerS4), anti-PD-L1 therapy (n = 4 SCR and n = 6 CerS4), or a combination (n = 5 SCR and n = 6 CerS4). (L) 4T1 allografts stably expressing SCR (n = 8) or CerS4 (n = 8) shRNA were established in BALB/c mice unilaterally. Tumors were collected after 21 days. Immune cells were characterized in the tumor microenvironment using spectral flow cytometry. (M) Tumor-infiltrating lymphocytes (TILs) were isolated from shSCR (n = 6) or shCerS4-transfected (n = 6) tumors from (L). TILs were cultured with anti-CD3 and anti-CD28 for 24 h before being treated with Golgi-stop for 3 h and processed for spectral flow cytometry. (N) Tumor-infiltrating lymphocytes (TILs) were analyzed in primary tumors from the vehicle or combination groups by performing multiplexed immunofluorescence using anti-CD3, anti-CD8, anti-FoxP3, and anti-PanCK antibodies. Scale bars, 20 μm. (O) Quantification of TIL populations counted from mulitplexed immunofluoresence shown in (N) is shown in lower panels (n = 4).

Data represent means ± SD; tumor growth data and metastasis quantification, means ± SEM; data from (L) and (M), means ± interquartile range. Student's t test, two-way ANOVA, or one-way ANOVA were used to determine significance: $^*p < 0.05$, $^{**}p < 0.01$, $^{***}p < 0.001$, $^{****}p < 0.0001$; ns, not significant.

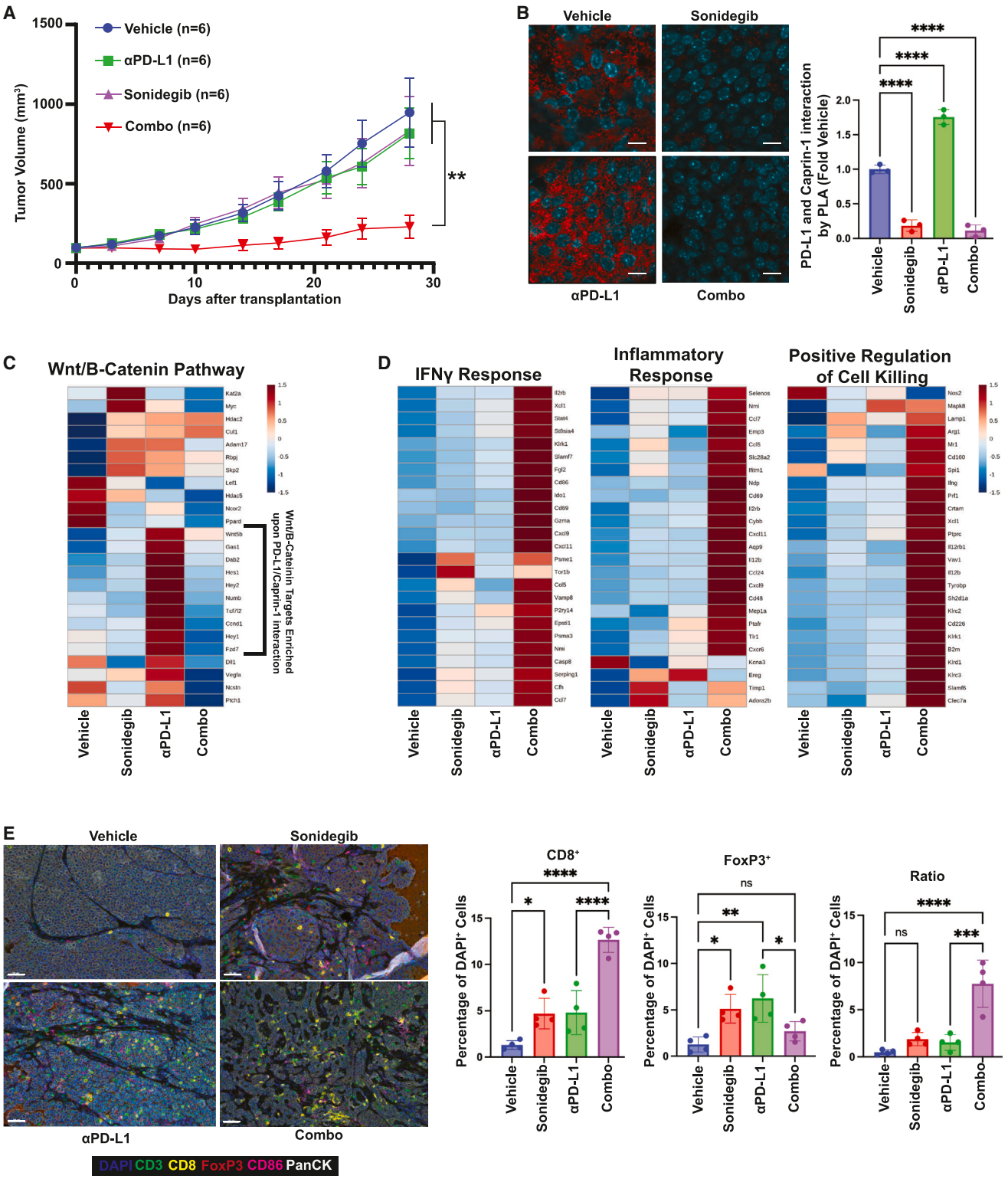

Figure 6. The CerS4/PD-L1/caprin-1 axis inhibition sensitizes TNBC tumors to immunotherapy

Metastatic PyMT tumors were established in FVB mice. After the tumors had formed, the mice were treated with vehicle, sonidegib, anti-PD-L1 therapy, or a combination for 28 days.

(A) Primary tumors were measured with calipers twice weekly, and tumor volumes were calculated (n = 6).

(legend continued on next page)

sonidegib + anti-PD-L1 (Combo) treatment slightly inhibited primary breast tumor growth (Figure 5F). Collected primary and metastatic tumors showed that sonidegib + anti-PD-L1 (Combo) treatment inhibited internalization of PD-L1 and Shh activation measured by PLA for PD-L1/caprin-1 and Shh-PTCH1 interactions compared to vehicle-treated controls (Figures 5G, 5H, and S5E). These data were also consistent with decreased Shh and TGFBR1 abundance in response to sonidegib + anti-PD-L1 (Combo) treatment in primary and metastatic shCerS4 tumors compared to vehicle-treated and single-agent-treated tumors (Figures 5I and S5F–S5H). Moreover, sonidegib + anti-PD-L1 (Combo) treatment abrogated the abundance of Wnt5b, Wnt7a, TCF7L2, and CTNNB1, which are involved in the activation of the Wnt/β-catenin signaling, in shCerS4 tumors compared to vehicle-treated controls (Figures 5J, 5K; S5I, and S5J). Since our data suggested that FoxP3$^+$ Treg abundance may mediate immune suppression in response to downregulation of CerS4 in 4T1-derived tumors, we further characterized immune cell populations in shSCR and shCerS4-transfected 4T1 breast tumors by flow cytometry. In this model, we detected a significant increase in the abundance of FoxP3$^+$ Tregs in breast tumors with CerS4 knockdown compared to SCR-shRNA-transfected tumors (Figure 5L). Moreover, the data showed a significant abundance of exhausted (PD1$^+$ TIM3$^+$ Lag3$^+$) CD4$^+$ and CD8$^+$ T cells in response to downregulation of CerS4 (Figure 5L). In CerS4-knockdown tumors, while lymphocyte populations were generally reduced, there were increases in specific myeloid populations, specifically Ly6G$^+$ cells, associated with myeloid-derived suppressor cells (MDSCs) (Figure S5K).

To examine the functional status of immune cells, we isolated tumor-infiltrated lymphocytes (TILs) from 4T1-derived tumors implanted into the mammary pads of Balb/c mice transfected with SCR- or CerS4-shRNAs. After activation *ex vivo*, T cell functions were analyzed using flow cytometry. T cells from shCerS4-transfected tumors were less inflammatory compared to shSCR tumors with decreased tumor necrosis factor α (TNF-α) production and increased interleukin-10 (IL-10) production compared to T cells isolated from SCR-shRNA-transfected tumors *ex vivo* (Figures 5M and S5L). These data suggest an immune-suppressive tumor microenvironment with increased FoxP3$^+$ Tregs and reduced CD8$^+$ T cell effector function in response to CerS4 downregulation. Sonidegib + anti-PD-L1 (Combo) treatment increased CD8$^+$ T cells while reducing FoxP3$^+$ Tregs in these tumors, resulting in enhanced anti-tumor immunity compared to vehicle-treated controls (Figures 5N, 5O, and S5M).

To validate the *in vivo* efficacy of sonidegib and anti-PD-L1 combination treatment, we used metastatic-stage MMTV-PyMT derived tumors implanted into FVB/n mice. Compared to early- or late-stage tumors, metastatic tumors had significantly more PD-L1 and Shh abundance and lower CerS4 levels (Figure S6A). After the tumors were grown to 90–100 mm^3, tumor-bearing mice were treated with vehicle, sonidegib, anti-PD-L1 antibody, or sonidegib + anti-PD-L1 antibody in combination (Combo) for 28 days. Treatment with the sonidegib + anti-PD-L1 antibody (Combo), but not the single agents, inhibited tumor growth compared to vehicle-treated controls (Figures 6A and S6B) without impacting body or spleen weights (Figures S6C and S6D). When we measured the effects of these treatments on PD-L1/caprin-1 association and Shh signaling, we observed that while anti-PD-L1 antibody as a single agent increased PD-L1/caprin-1 association and increased PTCH1, Gli1, and Shh abundance, sonidegib + anti-PD-L1 antibody in combination (Combo) reduced PD-L1/caprin-1 interaction, increased surface PD-L1 abundance, and inhibited Shh signaling compared to anti-PD-L1-treated tumors (Figures 6B, S6E, and S6F). These data suggest that Shh pathway activity is vital in PD-L1 internalization in response to CerS4 knockdown. Bulk mRNA sequencing using total RNA isolated from these tumors also demonstrated the inhibition of Shh signaling and Wnt/β-catenin in response to sonidegib + anti-PD-L1 antibody (Combo) in tumors compared to vehicle- or single-agent-treated tumors (Figures 6C and S6G). Since these pathways are targets of the CerS4/PD-L1/caprin-1 axis, we also determined whether other classical lipid metabolic pathways, such as the PPAR family or fatty acid metabolism, were affected by treatment and did not see any significant results (Figures S6H and S6I). RNA sequencing also showed that sonidegib + anti-PD-L1 antibody (Combo) treatment resulted in the activation of genes involved in favorable anti-tumor immune responses such as IFN-γ, inflammatory response, and positive cell killing compared to vehicle- or single-agent-treated tumors (Figure 6D). Activation of anti-tumor immune response by the sonidegib + anti-PD-L1 antibody (Combo) treatment was also validated by multiplex immunofluorescence, which showed an increased ratio between CD8$^+$ T cells and FoxP3$^+$ Tregs compared to vehicle- or single-agent-treated tumors (Figure 6E).

These data demonstrate that blockade of Shh signaling and PD-L1 using sonidegib + anti-PD-L1 antibody in combination inhibits breast tumor metastasis and growth, concomitant with inhibition of PD-L1 internalization, PD-L1/caprin-1 association, Shh, and Wnt/β-catenin signaling. These data also show that sonidegib + anti-PD-L1 antibody treatment improves the balance between CD8$^+$ effector T cell vs. FoxP3$^+$ Treg infiltration to the primary and metastatic breast tumor microenvironment, enhancing anti-tumor immunity in mice.

(B) Interaction between PD-L1 and caprin-1 was detected by PLA assay using anti-PD-L1 and anti-caprin-1 antibodies in primary tumors (n = 3). Scale bars, 10 μm.
(C) Pathway enrichment for Wnt/B-catenin signaling was performed after bulk RNA sequencing of the primary tumors using a suite of Wnt/B-catenin-related genes (n = 4).
(D) Pathway enrichment for IFN-γ response, inflammatory response, and positive regulation of cell killing was performed after bulk RNA sequencing of the primary tumors (n = 4).
(E) Immune cells in the primary tumor were analyzed by performing multiplexed immunofluorescence using anti-CD3, anti-CD8, anti-FoxP3, anti-CD86, and anti-PanCK antibodies (n = 4). Data quantification is shown in right panels. Scale bars, 50 μm.
Data represent means ± SD, tumor growth data represent means ± SEM; one-way ANOVA was used to determine significance: $^*p < 0.05$, $^{**}p < 0.01$, $^{***}p < 0.001$, $^{****}p < 0.0001$; ns, not significant.

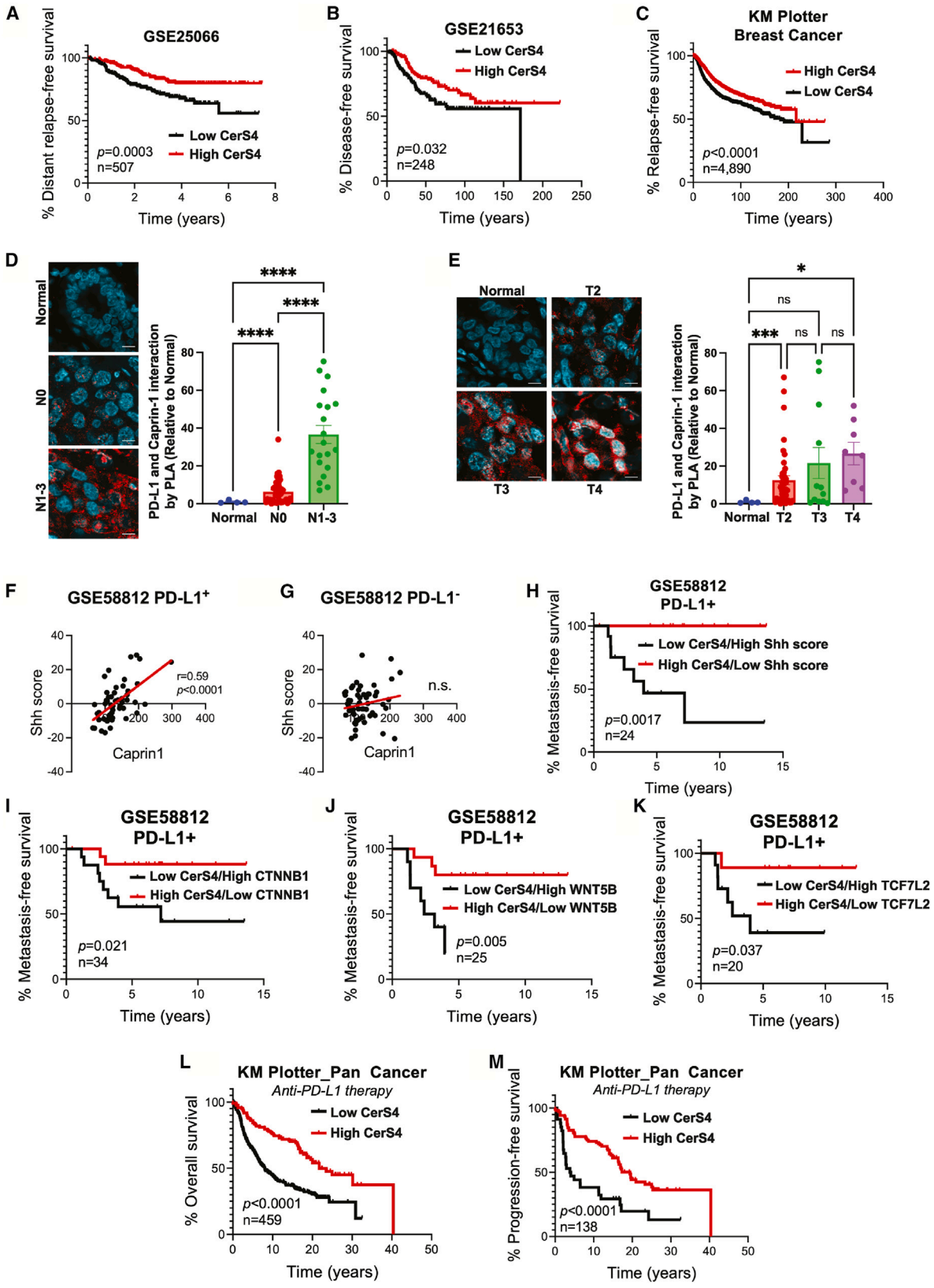

(legend on next page)

Clinical relevance of the CerS4-dependent PD-L1/caprin-1 and Shh/Wnt signaling alterations in breast cancer patients

We analyzed multiple breast cancer patient datasets and found that low levels of CERS4 are associated with significantly worse survival (both disease-free and distant-relapse-free) compared to high-Cers4-expressing breast cancer patients, thus demonstrating the clinical relevance of Cers4 alterations to breast cancer (Figures 7A–7C). Next, we examined PD-L1 internalization in a tumor microarray containing triple-negative breast tumors isolated from patients with N0 or N1–N3 stages of disease in addition to normal breast tissue. Measuring PD-L1/caprin-1 association by PLA demonstrated that PD-L1/caprin-1 association was highly increased in N1–N3 stage tumors compared to N0 or normal tissue (Figure 7D). When we measured PD-L1/caprin-1 interaction by PLA across different stages of TNBC (T2–T4), data showed higher levels of PD-L1/caprin-1 association compared to normal breast tissues but not between stages (Figure 7E).

To further test the clinical relevance of the CerS4/PD-L1/caprin-1/Shh axis in TNBCs, we analyzed a publicly available gene expression dataset of 107 TNBC patients (GSE58812). We generated an Shh pathway signaling score for each patient using genes in the Kyoto Encyclopedia of Genes and Genomes (KEGG) Hedgehog Signaling Pathways (STAR Methods). Patients were then stratified by their PD-L1 expression into positive (high) and negative (low) groups based on median PD-L1 expression. Caprin-1 is significantly positively correlated with Shh score only in PD-L1-positive patients but not in PD-L1-negative patients (Figures 7F and 7G). Survival analysis demonstrated that among PD-L1-positive TNBC patients, those expressing low levels of Cers4 but high levels of Shh score exhibit a much worse metastasis-free survival than those with high Cers4 and low Shh score (Figure 7H). Likewise, PD-L1-positive TNBC patients with low levels of Cers4 and high levels of the Wnt-related genes CTNNB1, Wnt5b, and TCF7L2, the latter involved in the crosstalk between Wnt and TGF-β signaling, had significantly worse metastasis-free survival compared to those with high-Cers4- and low-Wnt-related genes (Figures 7I–7K).[49] The separations of patient survival were more substantial compared to the effects of the individual genes (Figures S7A–S7E), suggesting that Cers4 is indeed in association with Shh/Wnt signaling pathway members in patient tumors. In the PD-L1-negative patients, individual or combined expressions of none of the genes resulted in a significant separation of metastasis-free survival (Figures S7F–S7N). Lastly, we performed pan-cancer survival analysis with anti-PD-L1 antibody-treated cancer patients and demonstrated significantly worse overall and progression-free survival in patients with low levels of Cers4 (Figures 7L and 7M). These data reveal that low levels of Cers4 and the subsequent activation of Shh/TGF-β/Wnt signaling pathways upon PDL1/caprin-1 internalization predicts worse clinical outcomes, especially in TNBCs and specifically in patients treated with PD-L1-targeting therapies.

DISCUSSION

This study revealed that Shh/SMO/TGFBR1 activation in response to CerS4/ceramide inhibition is involved in the internalization of PD-L1, resulting in the formation of the intracellular PD-L1/caprin-1 complex, stimulating expression of Wnt/β-catenin-related genes and inducing migration and metastasis of TNBCs. Targeting the Shh pathway, which prevented PD-L1 internalization, plus inhibition of PD-L1 in mice with metastatic breast tumors in the absence/presence of CerS4 knockdown by using sonidegib + anti-PD-L1 antibody largely inhibited breast tumor growth and lung metastasis. The sonidegib and anti-PD-L1 antibody combination also reversed $CD8^+$ T effector/$FoxP3^+$ Treg ratios in metastatic breast tumors, enhancing response to immunotherapy. Our patient data analyses revealed a high clinical relevance of the identified low CerS4 and high PD-L1/caprin-1 and Shh/TGF-β/Wnt axis and their association with decreased overall survival and metastasis-free survival in patients with TNBCs.

Shh signaling plays a vital role in organogenesis, tissue regeneration, and stem cell renewal.[50,51] Aberrantly increased Shh activation is associated with various solid tumors, such as melanoma and brain, breast, colon, liver, lung, or pancreatic

Figure 7. Clinical relevance of the CerS4-dependent PD-L1/caprin-1 and Shh/Wnt signaling alterations

(A) Kaplan-Meier survival curve representing the percentage of distant relapse-free survival in breast cancer patients from GSE25066 (n = 507) separated based on low vs. high CerS4 mRNA expression.

(B) Kaplan-Meier survival curve representing the percentage of disease-free survival in breast cancer patients from GSE21653 (n = 248).

(C) Kaplan-Meier survival curve representing the percentage relapse-free survival in breast cancer patients from KM-Plotter (n = 4,890).

(D and E) Interaction between PD-L1 and caprin-1 was detected by PLA using anti-PD-L1 and anti-caprin-1 antibodies in a commercially available tissue microarray containing normal breast tissue (n = 4 patients) and TNBC primary tumors (n = 62 patients). Two images were taken per tissue core, and two cores were present per patient sample.

(D) Interaction between PD-L1 and caprin-1 was quantified in normal breast tissue (n = 4), lymph-node-negative primary tumors (N0, n = 42), and lymph-node-positive primary tumors (N1–N3, n = 20). Scale bars, 10 μm.

(E) Interaction between PD-L1 and caprin-1 was quantified in normal breast tissue (n = 4), stage 2 primary tumors (T2, n = 42), stage 3 primary tumors (T3, n = 12), and stage 4 primary tumors (T4, n = 8). Scale bars, 10 μm.

(F and G) Correlation analysis of caprin-1 mRNA expression and Shh score in TNBC patients from GSE58812 (n = 53 for PD-$L1^+$ [F], and n = 54 for PD-L1 [G]).

(H) Kaplan-Meier survival curve representing the percentage metastasis-free survival in PD-$L1^+$ TNBC patients from GSE58812 (n = 24) separated based on low vs. high CerS4 mRNA and Shh score.

(I–K) Kaplan-Meier survival curves representing the percentage metastasis-free survival in PD-$L1^+$ TNBC patients from GSE58812 (n = 20) separated based on low vs. high Cers4 and CTNNB1 (I), Wnt5b (J), or TCF7L2 (K) mRNA levels.

(L and M) Kaplan-Meier survival curves representing the percentage overall survival (L) and progression-free survival (M) in cancer patients treated with PD-L1 immunotherapy (n = 459 for overall survival and n = 138 for progression-free survival) separated based on low vs. high CerS4 mRNA expression. One-way ANOVA or log-rank test was used to determine significance: $^*p < 0.05$, $^{**}p < 0.01$, $^{***}p < 0.001$, $^{****}p < 0.0001$; ns, not significant.

cancers.[52–55] Thus, the Shh signaling inhibitors have been used to treat various cancer types in preclinical and clinical studies.[56] The canonical Shh pathway is regulated in primary cilia.[8,57] However, mechanisms that regulate Shh/PD-L1-mediated signaling for inducing tumor metastasis are largely unknown.

PD-L1 inhibits the functions of cytotoxic T cells via signaling through PD-1, exhibiting checkpoint block for T cells.[58,59] However, resistance to immunotherapy is a main obstacle to metastatic TNBC therapy.[60] Several intrinsic mechanisms are involved in the immunotherapy resistance, such as loss of antigen-presenting β2-microglobulin and expression levels of PD-L1 in TNBC cells.[61–63] Moreover, elevated PD-L1 expression correlates with increased response to immunotherapy.[64] In addition to its immune-suppressive functions, PD-L1 has additional pro-survival roles in tumor cells.[65] Intracellular roles of PD-L1 in response to CerS4 knockdown and activation of Shh signaling for inducing TNBC migration and metastasis have not been described previously. Our data here describe a mechanism whereby the PD-L1/caprin-1 complex provides a regulatory signaling platform to induce the expression and signaling of Shh, leading to enhanced metastasis.

Caprin-1 is associated with G3BP1 through its FGDF-(Phe-Gly-Asp-Phe) motif, which induces stress-granule formation.[66] Overexpression of caprin-1 also induces stress-granule formation.[67] Our studies did not demonstrate any role for intracellular PD-L1 in inducing caprin-1-dependent stress granules. However, our data revealed that internalization of PD-L1 in response to CerS4 knockdown induced the formation of the PD-L1/caprin-1 complex, which then induced caprin-1 binding to various mRNAs, including Shh, TGFBR1, and Wnt-related mRNAs. Inhibition of Wnt/β-catenin using pharmacologic inhibitors also abrogated breast cancer cell migration without influencing PD-L1/caprin-1 interaction.

These data have significant biological and therapeutic implications. We showed here that the combination of anti-PD-L1 antibody with sonidegib limited the metastatic potential of breast tumors and enhanced anti-tumor immune response *in vivo*. Also, we demonstrated that low CerS4 expression in combination with high levels of Shh/TGF-β/Wnt signaling is associated with significantly worse distant metastasis-free survival for TNBC patients. Furthermore, the clinical correlation between caprin-1 and Shh and the effect of CerS4 on distant relapse were confined to the cohort of breast cancer patients highly expressing PD-L1, demonstrating the vital relevance of the proposed axis to clinical outcomes. Although this study is focused on metastatic TNBCs, the data presented here might be relevant to other metastatic solid tumors, such as prostate, pancreatic, lung, or head and neck cancers, where caprin-1 overexpression or CerS4 downregulation is linked to a poor prognosis in patients.[68,69]

Limitations of the study

It has been shown that T cell-specific KOs can independently affect tumor growth.[70] One limitation is using our global CerS4 KO models, which does not allow for the dissection of cell-type-specific effects that contribute to the observed phenotype. Another critical aspect not explored is the influence of altered ceramide synthesis on membrane polarity, a potentially significant factor in cancer cell behavior. Moreover, the lack of specific activators of CerS4 or direct inhibitors of caprin-1 also poses a limitation. Lastly, the approaches for studying other major lipid metabolic pathways, such as cholesterol or phospholipids, beyond sphingolipids, might help capture the complexity of cellular processes, including migration/metastasis and immune suppression, in future studies.

Nevertheless, this study provides a mechanism that regulates breast cancer metastasis by internalizing PD-L1 to mediate TNBC metastasis and immune suppression. Our data also demonstrate that targeting Shh by sonidegib that inhibits PD-L1 internalization, in combination with an anti-PD-L1 antibody, presents a promising therapeutic strategy for patients with metastatic TNBCs or immunotherapy-resistant solid tumors with low CerS4 to improve response to immunotherapy.

STAR★METHODS

Detailed methods are provided in the online version of this paper and include the following:

- KEY RESOURCES TABLE
- RESOURCE AVAILABILITY
  - Lead contact
  - Materials availability
  - Data and code availability
- EXPERIMENTAL MODEL AND SUBJECT DETAILS
  - Animals
  - 4T1 orthotopic model and metastasis analysis
  - MMTV-PyMT metastatic mammary tumor model
  - Generation of MMTV-PyMT/CerS4$^{-/-}$ mice and analysis of lung metastasis
  - Cell lines and culture conditions
- METHOD DETAILS
  - Plasmids and antibodies
  - Cellular migration assay and analysis
  - Measurement of ceramides by LC/MS/MS
  - Immunofluorescence and immunohistochemistry
  - Proximity ligand assay (PLA) studies
  - Immunoblotting
  - Immunoprecipitation
  - Quantitative PCR
  - RNA-immunoprecipitation coupled RT-qPCR
  - RNA-immunoprecipitation sequencing
  - Whole-transcriptome sequencing (RNA-seq)
  - mRNA stability assays
  - Protein sequence analysis by LC-MS/MS
  - Isolation and activation of tumor-infiltrating lymphocytes (TILs)
  - Treatment with anti-PD-L1 and sonidegib *in vivo*
- QUANTIFICATION AND STATISTICAL ANALYSIS
  - Multiplex staining and scanning
  - Flow cytometry staining and analysis
  - Statistical analyses
  - Patient data analyses

SUPPLEMENTAL INFORMATION

Supplemental information can be found online at https://doi.org/10.1016/j.celrep.2024.114532.

ACKNOWLEDGMENTS

We thank the members of the Ogretmen Laboratory for their helpful discussions. This work was supported by research funding from the National

Institutes of Health (CA214461, DE016572, and P01 CA203628 to B.O.). The core facilities utilized are supported by NIH (C06 RR015455 and Hollings Cancer Center support grant P30 CA138313).

AUTHOR CONTRIBUTIONS

Conception and design, W.W., J.K., and B.O.; methodology development, W.W., J.K., D.K., N.O., and B.O.; data acquisition, W.W., J.K., D.K., A.H.J., H.G.L., F.C.A., N.O., M.F.K., O.S., P.C., S.G., B.H., P.H., S.M., O.S., and B.O.; data analysis and interpretation, W.W., J.K., H.L., O.S., U.M.T., and B.O.; manuscript writing, review, and revision, W.W., J.K., and B.O.; administrative, technical, or material support, W.W., J.K., and B.O.; study supervision, B.O.

DECLARATION OF INTERESTS

The authors declare no competing interests.

Received: January 9, 2024
Revised: May 17, 2024
Accepted: July 9, 2024

REFERENCES

1. Wells, A., Grahovac, J., Wheeler, S., Ma, B., and Lauffenburger, D. (2013). Targeting tumor cell motility as a strategy against invasion and metastasis. Trends Pharmacol. Sci. *34*, 283–289. https://doi.org/10.1016/j.tips.2013.03.001.
2. Muthuswamy, S.K. (2021). Self-organization in cancer: Implications for histopathology, cancer cell biology, and metastasis. Cancer Cell *39*, 443–446. https://doi.org/10.1016/j.ccell.2021.01.010.
3. Jakowlew, S.B. (2006). Transforming growth factor-beta in cancer and metastasis. Cancer Metastasis Rev. *25*, 435–457. https://doi.org/10.1007/s10555-006-9006-2.
4. Xu, J., Acharya, S., Sahin, O., Zhang, Q., Saito, Y., Yao, J., Wang, H., Li, P., Zhang, L., Lowery, F.J., et al. (2015). 14-3-3ζ turns TGF-β's function from tumor suppressor to metastasis promoter in breast cancer by contextual changes of Smad partners from p53 to Gli2. Cancer Cell *27*, 177–192. https://doi.org/10.1016/j.ccell.2014.11.025.
5. Riaz, S.K., Ke, Y., Wang, F., Kayani, M.A., and Malik, M.F.A. (2019). Influence of SHH/GLI1 axis on EMT mediated migration and invasion of breast cancer cells. Sci. Rep. *9*, 6620. https://doi.org/10.1038/s41598-019-43093-x.
6. Bailey, J.M., Mohr, A.M., and Hollingsworth, M.A. (2009). Sonic hedgehog paracrine signaling regulates metastasis and lymphangiogenesis in pancreatic cancer. Oncogene *28*, 3513–3525. https://doi.org/10.1038/onc.2009.220.
7. Yao, Z., Han, L., Chen, Y., He, F., Sun, B., Kamar, S., Zhang, Y., Yang, Y., Wang, C., and Yang, Z. (2018). Hedgehog signalling in the tumourigenesis and metastasis of osteosarcoma, and its potential value in the clinical therapy of osteosarcoma. Cell Death Dis. *9*, 701. https://doi.org/10.1038/s41419-018-0647-1.
8. Corbit, K.C., Aanstad, P., Singla, V., Norman, A.R., Stainier, D.Y.R., and Reiter, J.F. (2005). Vertebrate Smoothened functions at the primary cilium. Nature *437*, 1018–1021. https://doi.org/10.1038/nature04117.
9. Li, S., Li, S., Wang, B., and Jiang, J. (2018). Hedgehog reciprocally controls trafficking of Smo and Ptc through the Smurf family of E3 ubiquitin ligases. Sci. Signal. *11*, eaan8660. https://doi.org/10.1126/scisignal.aan8660.
10. Bhateja, P., Cherian, M., Majumder, S., and Ramaswamy, B. (2019). The Hedgehog Signaling Pathway: A Viable Target in Breast Cancer? Cancers *11*, 1126. https://doi.org/10.3390/cancers11081126.
11. Liu, S., Ren, J., and ten Dijke, P. (2021). Targeting TGFβ signal transduction for cancer therapy. Signal Transduct. Target. Ther. *6*, 8. https://doi.org/10.1038/s41392-020-00436-9.
12. Robert, C. (2020). A decade of immune-checkpoint inhibitors in cancer therapy. Nat. Commun. *11*, 3801. https://doi.org/10.1038/s41467-020-17670-y.
13. Lai, X., Stiff, A., Duggan, M., Wesolowski, R., Carson, W.E., 3rd, and Friedman, A. (2018). Modeling combination therapy for breast cancer with BET and immune checkpoint inhibitors. Proc. Natl. Acad. Sci. USA *115*, 5534–5539. https://doi.org/10.1073/pnas.1721559115.
14. Onishi, H., Fujimura, A., Oyama, Y., Yamasaki, A., Imaizumi, A., Kawamoto, M., Katano, M., Umebayashi, M., and Morisaki, T. (2016). Hedgehog signaling regulates PDL-1 expression in cancer cells to induce anti-tumor activity by activated lymphocytes. Cell. Immunol. *310*, 199–204. https://doi.org/10.1016/j.cellimm.2016.08.003.
15. Topalian, S.L., Hodi, F.S., Brahmer, J.R., Gettinger, S.N., Smith, D.C., McDermott, D.F., Powderly, J.D., Carvajal, R.D., Sosman, J.A., Atkins, M.B., et al. (2012). Safety, activity, and immune correlates of anti-PD-1 antibody in cancer. N. Engl. J. Med. *366*, 2443–2454. https://doi.org/10.1056/NEJMoa1200690.
16. Sun, L., Zhang, L., Yu, J., Zhang, Y., Pang, X., Ma, C., Shen, M., Ruan, S., Wasan, H.S., and Qiu, S. (2020). Clinical efficacy and safety of anti-PD-1/PD-L1 inhibitors for the treatment of advanced or metastatic cancer: a systematic review and meta-analysis. Sci. Rep. *10*, 2083. https://doi.org/10.1038/s41598-020-58674-4.
17. Weinstock, M., and McDermott, D. (2015). Targeting PD-1/PD-L1 in the treatment of metastatic renal cell carcinoma. Ther. Adv. Urol. *7*, 365–377. https://doi.org/10.1177/1756287215597647.
18. Sharpe, A.H., and Pauken, K.E. (2018). The diverse functions of the PD1 inhibitory pathway. Nat. Rev. Immunol. *18*, 153–167. https://doi.org/10.1038/nri.2017.108.
19. George, J., Saito, M., Tsuta, K., Iwakawa, R., Shiraishi, K., Scheel, A.H., Uchida, S., Watanabe, S.I., Nishikawa, R., Noguchi, M., et al. (2017). Genomic Amplification of CD274 (PD-L1) in Small-Cell Lung Cancer. Clin. Cancer Res. *23*, 1220–1226. https://doi.org/10.1158/1078-0432.Ccr-16-1069.
20. Yamaguchi, H., Hsu, J.-M., Yang, W.-H., and Hung, M.-C. (2022). Mechanisms regulating PD-L1 expression in cancers and associated opportunities for novel small-molecule therapeutics. Nat. Rev. Clin. Oncol. *19*, 287–305. https://doi.org/10.1038/s41571-022-00601-9.
21. Perrichet, A., Ghiringhelli, F., and Rébé, C. (2020). Understanding Inflammasomes and PD-1/PD-L1 Crosstalk to Improve Cancer Treatment Efficiency. Cancers *12*, 3550. https://doi.org/10.3390/cancers12123550.
22. Tu, X., Qin, B., Zhang, Y., Zhang, C., Kahila, M., Nowsheen, S., Yin, P., Yuan, J., Pei, H., Li, H., et al. (2019). PD-L1 (B7-H1) Competes with the RNA Exosome to Regulate the DNA Damage Response and Can Be Targeted to Sensitize to Radiation or Chemotherapy. Mol. Cell *74*, 1215–1226.e4. https://doi.org/10.1016/j.molcel.2019.04.005.
23. Sun, L., Wang, Y., Wang, X., Navarro-Corcuera, A., Ilyas, S., Jalan-Sakrikar, N., Gan, C., Tu, X., Shi, Y., Tu, K., et al. (2022). PD-L1 promotes myofibroblastic activation of hepatic stellate cells by distinct mechanisms selective for TGF-β receptor I versus II. Cell Rep. *38*, 110349. https://doi.org/10.1016/j.celrep.2022.110349.
24. Oakley, R.H., Laporte, S.A., Holt, J.A., Barak, L.S., and Caron, M.G. (2001). Molecular determinants underlying the formation of stable intracellular G protein-coupled receptor-beta-arrestin complexes after receptor endocytosis. J. Biol. Chem. *276*, 19452–19460. https://doi.org/10.1074/jbc.M101450200.
25. Shi, Y., and Massagué, J. (2003). Mechanisms of TGF-β Signaling from Cell Membrane to the Nucleus. Cell *113*, 685–700. https://doi.org/10.1016/S0092-8674(03)00432-X.
26. Ruiz-Gómez, A., Molnar, C., Holguín, H., Mayor, F., and de Celis, J.F. (2007). The cell biology of Smo signalling and its relationships with GPCRs.

Biochim. Biophys. Acta *1768*, 901–912. https://doi.org/10.1016/j.bbamem.2006.09.020.

27. Hannun, Y.A., and Bell, R.M. (1989). Functions of Sphingolipids and Sphingolipid Breakdown Products in Cellular Regulation. Science *243*, 500–507. https://doi.org/10.1126/science.2643164.
28. Ogretmen, B. (2018). Sphingolipid metabolism in cancer signalling and therapy. Nat. Rev. Cancer *18*, 33–50. https://doi.org/10.1038/nrc.2017.96.
29. Obeid, L.M., Linardic, C.M., Karolak, L.A., and Hannun, Y.A. (1993). Programmed cell death induced by ceramide. Science *259*, 1769–1771. https://doi.org/10.1126/science.8456305.
30. Ogretmen, B., and Hannun, Y.A. (2004). Biologically active sphingolipids in cancer pathogenesis and treatment. Nat. Rev. Cancer *4*, 604–616. https://doi.org/10.1038/nrc1411.
31. Tidhar, R., Zelnik, I.D., Volpert, G., Ben-Dor, S., Kelly, S., Merrill, A.H., Jr., and Futerman, A.H. (2018). Eleven residues determine the acyl chain specificity of ceramide synthases. J. Biol. Chem. *293*, 9912–9921. https://doi.org/10.1074/jbc.RA118.001936.
32. Levy, M., and Futerman, A.H. (2010). Mammalian ceramide synthases. IUBMB Life *62*, 347–356. https://doi.org/10.1002/iub.319.
33. Hartmann, D., Lucks, J., Fuchs, S., Schiffmann, S., Schreiber, Y., Ferrerirós, N., Merkens, J., Marschalek, R., Geisslinger, G., and Grösch, S. (2012). Long chain ceramides and very long chain ceramides have opposite effects on human breast and colon cancer cell growth. Int. J. Biochem. Cell Biol. *44*, 620–628. https://doi.org/10.1016/j.biocel.2011.12.019.
34. Gencer, S., Oleinik, N., Kim, J., Panneer Selvam, S., De Palma, R., Dany, M., Nganga, R., Thomas, R.J., Senkal, C.E., Howe, P.H., and Ogretmen, B. (2017). TGF-β receptor I/II trafficking and signaling at primary cilia are inhibited by ceramide to attenuate cell migration and tumor metastasis. Sci. Signal. *10*, eaam7464. https://doi.org/10.1126/scisignal.aam7464.
35. Liu, Y., Cao, X., Jiang, J., and Jia, J. (2007). Fused-Costal2 protein complex regulates Hedgehog-induced Smo phosphorylation and cell-surface accumulation. Genes Dev. *21*, 1949–1963. https://doi.org/10.1101/gad.1557407.
36. Kupinski, A.P., Raabe, I., Michel, M., Ail, D., Brusch, L., Weidemann, T., and Bökel, C. (2013). Phosphorylation of the Smo tail is controlled by membrane localisation and is dispensable for clustering. J. Cell Sci. *126*, 4684–4697. https://doi.org/10.1242/jcs.128926.
37. Jia, H., Liu, Y., Yan, W., and Jia, J. (2009). PP4 and PP2A regulate Hedgehog signaling by controlling Smo and Ci phosphorylation. Development *136*, 307–316. https://doi.org/10.1242/dev.030015.
38. Yu, W., Hua, Y., Qiu, H., Hao, J., Zou, K., Li, Z., Hu, S., Guo, P., Chen, M., Sui, S., et al. (2020). PD-L1 promotes tumor growth and progression by activating WIP and β-catenin signaling pathways and predicts poor prognosis in lung cancer. Cell Death Dis. *11*, 506. https://doi.org/10.1038/s41419-020-2701-z.
39. Parvathareddy, S.K., Siraj, A.K., Al-Badawi, I.A., Tulbah, A., Al-Dayel, F., and Al-Kuraya, K.S. (2021). Differential expression of PD-L1 between primary and metastatic epithelial ovarian cancer and its clinico-pathological correlation. Sci. Rep. *11*, 3750. https://doi.org/10.1038/s41598-021-83276-z.
40. Cirqueira, M.B., Mendonça, C.R., Noll, M., Soares, L.R., de Paula Carneiro Cysneiros, M.A., Paulinelli, R.R., Moreira, M.A.R., and Freitas-Junior, R. (2021). Prognostic Role of PD-L1 Expression in Invasive Breast Cancer: A Systematic Review and Meta-Analysis. Cancers *13*, 6090. https://doi.org/10.3390/cancers13236090.
41. Miles, D., Gligorov, J., André, F., Cameron, D., Schneeweiss, A., Barrios, C., Xu, B., Wardley, A., Kaen, D., Andrade, L., et al. (2021). Primary results from IMpassion131, a double-blind, placebo-controlled, randomised phase III trial of first-line paclitaxel with or without atezolizumab for unresectable locally advanced/metastatic triple-negative breast cancer. Ann. Oncol. *32*, 994–1004. https://doi.org/10.1016/j.annonc.2021.05.801.
42. Chew, H.Y., De Lima, P.O., Gonzalez Cruz, J.L., Banushi, B., Echejoh, G., Hu, L., Joseph, S.R., Lum, B., Rae, J., O'Donnell, J.S., et al. (2020). Endocytosis Inhibition in Humans to Improve Responses to ADCC-Mediating Antibodies. Cell *180*, 895–914.e27. https://doi.org/10.1016/j.cell.2020.02.019.
43. Tseng, Y.J., Lee, C.H., Chen, W.Y., Yang, J.L., and Tzeng, H.T. (2021). Inhibition of PAI-1 Blocks PD-L1 Endocytosis and Improves the Response of Melanoma Cells to Immune Checkpoint Blockade. J. Invest. Dermatol. *141*, 2690–2698.e6. https://doi.org/10.1016/j.jid.2021.03.030.
44. Gao, Y., Nihira, N.T., Bu, X., Chu, C., Zhang, J., Kolodziejczyk, A., Fan, Y., Chan, N.T., Ma, L., Liu, J., et al. (2020). Acetylation-dependent regulation of PD-L1 nuclear translocation dictates the efficacy of anti-PD-1 immunotherapy. Nat. Cell Biol. *22*, 1064–1075. https://doi.org/10.1038/s41556-020-0562-4.
45. Gong, B., Hu, H., Chen, J., Cao, S., Yu, J., Xue, J., Chen, F., Cai, Y., He, H., and Zhang, L. (2013). Caprin-1 is a novel microRNA-223 target for regulating the proliferation and invasion of human breast cancer cells. Biomed. Pharmacother. *67*, 629–636. https://doi.org/10.1016/j.biopha.2013.06.006.
46. Guo, X.M., Zhu, F.F., Pan, L.W., Chen, J.L., Lai, J.C., Wu, H.X., and Shu, J.C. (2020). Caprin-1 promotes HepG2 cell proliferation, invasion and migration and is associated with poor prognosis in patients with liver cancer. Oncol. Lett. *20*, 1761–1771. https://doi.org/10.3892/ol.2020.11712.
47. Song, D., Kuang, L., Yang, L., Wang, L., Li, H., Li, X., Zhu, Z., Shi, C., Zhu, H., and Gong, W. (2022). Yin and yang regulation of stress granules by Caprin-1. Proc. Natl. Acad. Sci. USA *119*, e2207975119. https://doi.org/10.1073/pnas.2207975119.
48. Marcelo, A., Koppenol, R., de Almeida, L.P., Matos, C.A., and Nóbrega, C. (2021). Stress granules, RNA-binding proteins and polyglutamine diseases: too much aggregation? Cell Death Dis. *12*, 592. https://doi.org/10.1038/s41419-021-03873-8.
49. Nakano, N., Itoh, S., Watanabe, Y., Maeyama, K., Itoh, F., and Kato, M. (2010). Requirement of TCF7L2 for TGF-beta-dependent transcriptional activation of the TMEPAI gene. J. Biol. Chem. *285*, 38023–38033. https://doi.org/10.1074/jbc.M110.132209.
50. Ebel, P., Imgrund, S., Vom Dorp, K., Hofmann, K., Maier, H., Drake, H., Degen, J., Dörmann, P., Eckhardt, M., Franz, T., and Willecke, K. (2014). Ceramide synthase 4 deficiency in mice causes lipid alterations in sebum and results in alopecia. Biochem. J. *461*, 147–158. https://doi.org/10.1042/bj20131242.
51. Hooper, J.E., and Scott, M.P. (2005). Communicating with Hedgehogs. Nat. Rev. Mol. Cell Biol. *6*, 306–317. https://doi.org/10.1038/nrm1622.
52. Jing, J., Wu, Z., Wang, J., Luo, G., Lin, H., Fan, Y., and Zhou, C. (2023). Hedgehog signaling in tissue homeostasis, cancers, and targeted therapies. Signal Transduct. Target. Ther. *8*, 315. https://doi.org/10.1038/s41392-023-01559-5.
53. Riobo-Del Galdo, N.A., Lara Montero, Á., and Wertheimer, E.V. (2019). Role of Hedgehog Signaling in Breast Cancer: Pathogenesis and Therapeutics. Cells *8*, 375. https://doi.org/10.3390/cells8040375.
54. Harris, L.G., Pannell, L.K., Singh, S., Samant, R.S., and Shevde, L.A. (2012). Increased vascularity and spontaneous metastasis of breast cancer by hedgehog signaling mediated upregulation of cyr61. Oncogene *31*, 3370–3380. https://doi.org/10.1038/onc.2011.496.
55. Chakrabarti, J., Holokai, L., Syu, L., Steele, N.G., Chang, J., Wang, J., Ahmed, S., Dlugosz, A., and Zavros, Y. (2018). Hedgehog signaling induces PD-L1 expression and tumor cell proliferation in gastric cancer. Oncotarget *9*, 37439–37457. https://doi.org/10.18632/oncotarget.26473.
56. Rubin, L.L., and de Sauvage, F.J. (2006). Targeting the Hedgehog pathway in cancer. Nat. Rev. Drug Discov. *5*, 1026–1033. https://doi.org/10.1038/nrd2086.
57. Gu, D., and Xie, J. (2015). Non-Canonical Hh Signaling in Cancer-Current Understanding and Future Directions. Cancers *7*, 1684–1698. https://doi.org/10.3390/cancers7030857.
58. Fife, B.T., Pauken, K.E., Eagar, T.N., Obu, T., Wu, J., Tang, Q., Azuma, M., Krummel, M.F., and Bluestone, J.A. (2009). Interactions between PD-1

and PD-L1 promote tolerance by blocking the TCR-induced stop signal. Nat. Immunol. *10*, 1185–1192. https://doi.org/10.1038/ni.1790.

59. Havel, J.J., Chowell, D., and Chan, T.A. (2019). The evolving landscape of biomarkers for checkpoint inhibitor immunotherapy. Nat. Rev. Cancer *19*, 133–150. https://doi.org/10.1038/s41568-019-0116-x.

60. Vikas, P., Borcherding, N., and Zhang, W. (2018). The clinical promise of immunotherapy in triple-negative breast cancer. Cancer Manag. Res. *10*, 6823–6833. https://doi.org/10.2147/cmar.S185176.

61. Sade-Feldman, M., Jiao, Y.J., Chen, J.H., Rooney, M.S., Barzily-Rokni, M., Eliane, J.-P., Bjorgaard, S.L., Hammond, M.R., Vitzthum, H., Blackmon, S.M., et al. (2017). Resistance to checkpoint blockade therapy through inactivation of antigen presentation. Nat. Commun. *8*, 1136. https://doi.org/10.1038/s41467-017-01062-w.

62. Saleh, R., Toor, S.M., Khalaf, S., and Elkord, E. (2019). Breast Cancer Cells and PD-1/PD-L1 Blockade Upregulate the Expression of PD-1, CTLA-4, TIM-3 and LAG-3 Immune Checkpoints in CD4(+) T Cells. Vaccines (Basel) *7*, 149. https://doi.org/10.3390/vaccines7040149.

63. Planes-Laine, G., Rochigneux, P., Bertucci, F., Chrétien, A.S., Viens, P., Sabatier, R., and Gonçalves, A. (2019). PD-1/PD-L1 Targeting in Breast Cancer: The First Clinical Evidences Are Emerging. A Literature Review. Cancers *11*, 1033. https://doi.org/10.3390/cancers11071033.

64. Cortes, J., Rugo, H.S., Cescon, D.W., Im, S.-A., Yusof, M.M., Gallardo, C., Lipatov, O., Barrios, C.H., Perez-Garcia, J., Iwata, H., et al. (2022). Pembrolizumab plus Chemotherapy in Advanced Triple-Negative Breast Cancer. N. Engl. J. Med. *387*, 217–226. https://doi.org/10.1056/NEJMoa2202809.

65. Klement, J.D., Redd, P.S., Lu, C., Merting, A.D., Poschel, D.B., Yang, D., Savage, N.M., Zhou, G., Munn, D.H., Fallon, P.G., and Liu, K. (2023). Tumor PD-L1 engages myeloid PD-1 to suppress type I interferon to impair cytotoxic T lymphocyte recruitment. Cancer Cell *41*, 620–636.e9. https://doi.org/10.1016/j.ccell.2023.02.005.

66. Towers, E.R., Kelly, J.J., Sud, R., Gale, J.E., and Dawson, S.J. (2011). Caprin-1 is a target of the deafness gene Pou4f3 and is recruited to stress granules in cochlear hair cells in response to ototoxic damage. J. Cell Sci. *124*, 1145–1155. https://doi.org/10.1242/jcs.076141.

67. Gal, J., Chen, J., Na, D.Y., Tichacek, L., Barnett, K.R., and Zhu, H. (2019). The Acetylation of Lysine-376 of G3BP1 Regulates RNA Binding and Stress Granule Dynamics. Mol. Cell Biol. *39*, e00052-19. https://doi.org/10.1128/mcb.00052-19.

68. Okano, F., Saito, T., Minamida, Y., Kobayashi, S., Ido, T., Miyauchi, Y., Wasai, U., Akazawa, D., Kume, M., Ishibashi, M., et al. (2023). Identification of Membrane-expressed CAPRIN-1 as a Novel and Universal Cancer Target, and Generation of a Therapeutic Anti-CAPRIN-1 Antibody TRK-950. Cancer Res. Commun. *3*, 640–658. https://doi.org/10.1158/2767-9764.Crc-22-0310.

69. Sheridan, M., and Ogretmen, B. (2021). The Role of Ceramide Metabolism and Signaling in the Regulation of Mitophagy and Cancer Therapy. Cancers *13*, 2475.

70. El-Hindi, K., Brachtendorf, S., Hartel, J.C., Oertel, S., Birod, K., Merz, N., Trautmann, S., Thomas, D., Weigert, A., Schäufele, T.J., et al. (2022). T-Cell-Specific CerS4 Depletion Prolonged Inflammation and Enhanced Tumor Burden in the AOM/DSS-Induced CAC Model. Int. J. Mol. Sci. *23*, 1866.

STAR★METHODS

KEY RESOURCES TABLE

REAGENT or RESOURCE	SOURCE	IDENTIFIER
Antibodies		
InVivoPlus Mab anti-mouse PD-L1 (B7-H1)	BioXCell	Clone: 10F.9G2; Cat# BP010; RRID:AB_2934050
BV421 anti-mouse CD3 Antibody	Biolegend	Clone: 17A2; Cat# 100228; RRID:AB_2562553
FITC anti-mouse CD4 Antibody	Biolegend	Clone: GK1.5; Cat# 100406; RRID:AB_312690
BV605 anti-mouse CD8a Antibody	Biolegend	Clone: 53–6.7; Cat# 100744; RRID:AB_2562609
BV785 anti-mouse CD45 Antibody	Biolegend	Clone: 30-F11; Cat# 103149; RRID:AB_2564590
BV421 anti-mouse PD-1 Antibody	Biolegend	Clone: RMP1-30; Cat# 109121; RRID:AB_2687080
PE anti-mouse LAG-3 Antibody	Biolegend	Clone: C9B7W; Cat# 125207; RRID:AB_2133344
APC anti-mouse TIM-3 Antibody	Biolegend	Clone: B8.2C12; Cat# 134008; RRID:AB_2562997
PE-Cy7 anti-mouse GRZB Antibody	Biolegend	Clone: QA18A28; Cat# 396409; RRID:AB_2801078
PE anti-mouse FoxP3 Antibody	Biolegend	Clone: 150D; Cat# 320008; RRID:AB_492980
APC-Cy7 anti-mouse TNF-a Antibody	Biolegend	Clone: MP6-XT22; Cat# 506343; RRID:AB_2565952
PE anti-mouse IFN-g Antibody	Biolegend	Clone: XMG1.2; Cat# 505808; RRID:AB_315401
APC anti-mouse IL-10 Antibody	Biolegend	Clone: JES5-16E3; Cat# 505007; RRID:AB_315362
FITC anti-mouse CD11b Antibody	Biolegend	Clone: M1/70; Cat# 101205; RRID:AB_312789
PE anti-mouse Ly6C Antibody	Biolegend	Clone: HK1.4; Cat# 128007; RRID:AB_1186133
APC-Cy7 anti-mouse Ly6G Antibody	Biolegend	Clone: 1A8; Cat# 127623; RRID:AB_10640819
PE-Cy7 anti-mouse F4/80 Antibody	Biolegend	Clone: BM8; Cat# 123114; RRID:AB_893478
BV421 anti-mouse CD25 Antibody	Biolegend	Clone: 3C7; Cat# 101923; RRID:AB_2810329
APC anti-mouse CD274 (PD-L1)	Biolegend	Clone: 10F.9G2; Cat# 124312; RRID:AB_10612935
APC anti-human CD274 (PD-L1)	Biolegend	Clone: 29E.2A3; Cat# 329708; RRID:AB_940360
Anti-Shh monoclonal Ab	Santa-Cruz	Clone: E−1; Cat# sc-365112; RRID:AB_10709580
Anti-Actin polyclonal Ab	Millipore-Sigma	Clone: polyclonal; Cat# A2066; RRID:AB_476693
Anti-SMO polyclonal Ab	Invitrogen	Clone: polyclonal; Cat# PA5-72395; RRID:AB_2718249
Anti-PTCH1 monoclonal Ab	Santa-Cruz	Clone: A-2; Cat# sc-518044
Anti-CerS4 monoclonal Ab	Santa-Cruz	Clone: D-6; Cat# sc-376497; RRID:AB_11151410
Anti-CypB monoclonal Ab	Cell Signaling Tech	Clone: D1V5J; Cat# 43603; RRID:AB_2799247
Anti-Caprin-1 polyclonal Ab	Proteintech	Clone: polyclonal; Cat# 15112-1-AP; RRID:AB_2070016
Anti-Caprin-1 monoclonal Ab	Proteintech	Clone: 6B10F11; Cat# 66352-1-Ig; RRID:AB_2881732
Anti-PD-L1 monoclonal Ab	Abcam	Clone: EPR20529; Cat# ab213480; RRID:AB_2773715
Anti-PD-L1 monoclonal Ab	Santa-Cruz	Clone: D-8; Cat# sc-518027
Anti-PD-L1 monoclonal Ab	Proteintech	Clone: 2B11D11; Cat# 66248-1-Ig; RRID:AB_2756526
Anti-ATP1A1 monoclonal Ab	Abcam	Clone: EP1845Y; Cat# ab76020; RRID:AB_1310695
Anti-TGFBR1 polyclonal Ab	Abcam	Clone: Polyclonal; Cat# ab31013; RRID:AB_778352
Anti-FLAG monoclonal Ab	Millipore-Sigma	Clone: M2; Cat# F1804; RRID:AB_262044
Anti-EXOSC10 polyclonal Ab	Proteintech	Clone: Polyclonal; Cat# 11178-1-AP; RRID:AB_2293792
Anti-CD3 polyclonal Ab	Agilent	Clone: Polyclonal; Cat# A0452; RRID:AB_2335677
Anti-CD8 alpha monoclonal Ab	Abcam	Clone: EPR21769; Cat# ab217344; RRID:AB_2890649
Anti-FoxP3 monoclonal Ab	Cell Signaling Tech	Clone: D6O8R; Cat# 12653; RRID:AB_2797979
Anti-CD86 monoclonal Ab	Cell Signaling Tech	Clone: E5W6H; Cat# 19589; RRID:AB_2892094
Anti-PanCK monoclonal Ab mix	Roche	Clone: AE1/AE3/PCK26; Cat# 760–2135; RRID:AB_2810237
Anti-Wnt5b polyclonal Ab	Abclonal	Clone: Polyclonal; Cat# A8313; RRID:AB_2772903
Anti-TCF7L2 polyclonal Ab	Cell Signaling Tech	Clone: C48H11; Cat# 2569; RRID:AB_2199816
Anti-Gli1 monoclonal Ab	Santa-Cruz	Clone: C-1; Cat# sc-515751; RRID:AB_2934097

(*Continued on next page*)

Continued

REAGENT or RESOURCE	SOURCE	IDENTIFIER
Anti-CLTC monoclonal Ab	Invitrogen	Clone: X22; Cat# MA1-065; RRID:AB_2083179
Anti-E-cadherin monoclonal Ab	Cell Signaling Tech	Clone: 24E10; Cat# 3195; RRID:AB_2291471
Anti-PABP monoclonal Ab	Santa-Cruz	Clone: 10E10; Cat# sc-32318; RRID:AB_628097
Normal rabbit IgG	Millipore-Sigma	Clone: polyclonal; Cat# 12–370; RRID:AB_145841
Rabbit TrueBlot®: Anti-Rabbit IgG HRP	Rockland	Cat# 18-8816-33; RRID:AB_2610848
Mouse TrueBlot® ULTRA: Anti-Mouse Ig HRP	Rockland	Cat# 18-8817-33; RRID:AB_2610851
Peroxidase AffiniPure Goat Anti-Rabbit IgG (H + L)	Rockland	Cat# 111-035-003; RRID:AB_2313567
Peroxidase AffiniPure Goat Anti-Mouse IgG (H + L)	Rockland	Cat# 115-035-003; RRID:AB_10015289
Alexa Fluor® 488 AffiniPure Donkey Anti-Rabbit IgG (H + L)	Rockland	Cat# 711-545-152; RRID:AB_2313584
InVivoMab anti-mouse CD3	BioXCell	Clone: 17A2; Cat# BE0002; RRID:AB_1107630
InVivoMab anti-mouse CD28	BioXCell	Clone: 37.51; Cat# BE0015-1; RRID:AB_1107624
Biological samples		
Breast cancer tissue array	Tissuearray.com	Cat# BR1902
Breast tissue array, normal	Tissuearray.com	Cat# BRN04a
Chemicals, peptides, and recombinant proteins		
RBC Lysis Buffer (10X)	Biolegend	Cat# 420301
Ficoll®-Paque PREMIUM 1.084	Cytiva	Cat# GE17-5446-02
2-Mercaptoethanol	Gibco	Cat# 21985023
rhIL2	NCI, Biological Resources Branch	https://ncifrederick.cancer.gov/research/brb/productDataSheets/cytokineHumanInterleukins/IL-2Bulk.aspx
Pierce™ IP Lysis Buffer	Thermo Fisher Scientific	Cat# 87788
Protease inhibitors	Thermo Fisher Scientific	Cat# 78430
Halt™ Phosphatase inhibitors single use 100X cocktail	Thermo Fisher Scientific	Cat# 78428
Protector RNase Inhibitor	Roche	Cat# 3335402001
DMEM	GE Healthcare, HyClone	Cat# SH30243.FS
Penicillin-Streptomycin	Corning	Cat# 30-001-CI
plasmocin prophylactic	Invivogen	Cat# ant-mpp
Fetal Bovine Serum (FBS)	Atlanta Biologicals	Cat# N8141-5G
Fetal Bovine Serum (FBS) tet-system approved	Gibco	Cat# A4736401
Actinomycin D	Selleckchem	Cat# S8964
Ly2157299	Selleckchem	Cat# S2230
Sonidegib	Selleckchem	Cat# S2151
E7386	Selleckchem	Cat# E1348
Tegatrabetan	Selleckchem	Cat #S0733
Pitstop2	Selleckchem	Cat# S9670
Recombinant Mouse IFN-gamma Protein	R&D systems	Cat# 485-MI-100
Recombinant Mouse Shh Protein	Lifespan Biosciences	Cat# LS-G375-25
Doxycycline hyclate	Millipore-Sigma	Cat# D5207
4% Paraformaldehyde	Boster	Cat# AR1068
Triton™ X-100	Sigma	Cat# T9284-100ML
Fibronectin from human plasma	Sigma	Cat# F2006
Tris based unmasking solution	VectorLabs	Cat# H-3301-250

(*Continued on next page*)

Continued

REAGENT or RESOURCE	SOURCE	IDENTIFIER
Vectashield hardset™ Antifade Mounting Media with DAPI	VectorLabs	Cat# H-1500-10
Critical commercial assays		
Tumor Dissociation Kit, mouse	Miltenyi Biotec	Cat# 130-096-730
gentleMACS™ Dissociator	Miltenyi Biotec	Cat# 130-093-235
gentleMACS™ C Tubes	Miltenyi Biotec	Cat# 130-093-237
BD BD GolgiStop™ Protein Transport Inhibitor (containing Monensin)	BD Biosciences	Cat# BDB554724
BD Cytofix/Cytoperm™ Fixation/Permeabilization Solution Kit	BD Biosciences	Cat# 554714
LIVE/DEAD™ Fixable Blue Dead Cell Stain Kit, for UV excitation	Invitrogen	Cat# L23105
TruStain FcX™ (anti-mouse CD16/32) Antibody	Biolegend	Cat# 101320
Effectene Transfection Reagent	Qiagen	Cat# 301427
Pierce™ 660nm Protein Assay Reagent	Thermo Fisher Scientific	Cat# 22660
Duolink *In Situ* PLA Probe Anti-Rabbit PLUS	Sigma	Cat# DUO92002-100RXN
Duolink® *In Situ* PLA® Probe Anti-Mouse MINUS	Sigma	Cat# DUO92004-100RXN
Duolink® *In Situ* Detection Reagents Red	Sigma	Cat# DUO92008-100RXN
RNeasy Mini Kit	Qiagen	Cat# 74106
Sso Advanced Universal Probes Supermix	BioRad	Cat# 172-5281
iScript cDNA Synthesis Kit	BioRad	Cat# 1708891
Mouse Sonic Hedgehog/Shh N Terminus Quantikine ELISA Kit	Novus Biologicals	Cat# MSHH00
Deposited data		
Bulk RNA sequencing data	This paper	GEO: GSE267312
Caprin-1 RIP sequencing data	This paper	GEO: GSE250637
EXSCO10 RIP sequencing data	This paper	GEO: GSE250638
Proteomics data	This paper	PRIDE: PXD053108
Original WB data	This paper	Mendeley Data, V1, https://doi.org/10.17632/f9wgj84d7z.1
Experimental models: Cell lines		
4T1	ATCC	Cat#: CRL-2539; RRID:CVCL_0125
MDA-MB-231	ATCC	Cat#: HTB-26; RRID:CVCL_0062
LM2-4175	Howe Lab	RRID:CVCL_5998
Experimental models: Organisms/strains		
Balb/c	Jackson Laboratory	Strain# 000651; RRID:IMSR_JAX:000651
FVB/N	Jackson Laboratory	Strain# 001800; RRID:IMSR_JAX:001800
B6.FVB-Tg(MMTV-PyVT)634Mul/LellJ	Jackson Laboratory	Strain# 022974; RRID:IMSR_JAX:022974
CerS4$^{+/-}$	Ogretmen's laboratory	Ogretmen's laboratory
CerS4$^{-/-}$	Ogretmen's laboratory	Ogretmen's laboratory
Oligonucleotides		
Human CerS4 Taqman® Probe	Thermo-Fisher	Assay ID: Hs00226114_m1
Mouse CerS4 Taqman® Probe	Thermo-Fisher	Assay ID: Mm00482658_m1
Mouse TGFBR1 Taqman® Probe	Thermo-Fisher	Assay ID: Mm00436964_m1
Human TGFBR1 Taqman® Probe	Thermo-Fisher	Assay ID: Hs00610320_m1
Human RPLP0 Taqman® Probe	Thermo-Fisher	Assay ID: Hs99999902_m1
Mouse Shh Taqman® Probe	Thermo-Fisher	Assay ID: Mm03053649_s1
Mouse Beta-Actin Taqman® Probe	Thermo-Fisher	Assay ID: Mm02619580_g1

(*Continued on next page*)

Continued

REAGENT or RESOURCE	SOURCE	IDENTIFIER
Human Shh Taqman® Probe	Thermo-Fisher	Assay ID: Hs00179843_m1
Mouse CTNNB1 Taqman® Probe	Thermo-Fisher	Assay ID: Mm00483039_m1
Mouse Wnt5b Taqman® Probe	Thermo-Fisher	Assay ID: Mm00437350_m1
Mouse TCF7L2 Taqman® Probe	Thermo-Fisher	Assay ID: Mm00501505_m1
Mouse Wnt7a Taqman® Probe	Thermo-Fisher	Assay ID: Mm00437356_m1
CerS4 Genotyping Forward Primer: AGA AGG GAC CCC ACT AAT GTA TGG	IDT, Coralville	N/A
CerS4 Genotyping Reverse Primer: GAA GAC ACA CAG AAA GTG ACA TGG	IDT, Coralville	N/A
PyMT Genotyping Forward Primer: GGA AGC AAG TAC TTC ACA AGG G	IDT, Coralville	N/A
PyMT Genotyping Reverse Primer: GGA AAG TCA CTA GGA GCA GGG	IDT, Coralville	N/A
Recombinant DNA		
pLV[shRNA]-Hygro-U6>mCaprin1[shRNA#1]	VectorBuilder	N/A
pLV[Exp]-Neo-CMV>mCd274 [NM_021893.3]*/FLAG	VectorBuilder	PD-L1 WT
pLV[Exp]-Neo-CMV>mCd274 [NM_021893.3*]*/FLAG	VectorBuilder	PD-L1 S278/279A
pLV[Exp]-CMV>tTS/rtTA/Hygro	VectorBuilder	N/A
pLV[Exp]-Puro-TRE>hCERS4[NM_024552.3]	VectorBuilder	N/A
pLKO.1[shRNA]-Puro-CMV>CerS4 [shRNA#1]	Millipore-Sigma	TRCN0000337886
pLKO.1[shRNA]-Puro-CMV>SCR [shRNA#1]	Millipore-Sigma	SHC002
pLKO.1[shRNA]-Puro-CMV>Shh [shRNA#1]	Millipore-Sigma	TRCN0000031061
pLKO.1[shRNA]-Puro-CMV>SMO [shRNA#1]	Millipore-Sigma	TRCN0000026245
pLKO.1[shRNA]-Puro-CMV>cd274 [shRNA#1]	Millipore-Sigma	TRCN0000068001
Software and algorithms		
FlowJo 10.9	TreeStar, OR	https://www.flowjo.com/solutions/flowjo/downloads/
Prism 10	GraphPad	https://www.graphpad.com/scientific-software/prism/
CFX Manager 3.1	Biorad	http://imagej.net/Fiji
Fiji	NIH Image	http://imagej.net/Fiji
FV10i	Olympus Corp.	FV10-ASW http://www.grapecity.com
Metaboanalyst 5.0	McGill University	https://www.metaboanalyst.ca
Partek Flow Bioinformatics Software	Partek	www.partek.com
Duolink *in Situ* Image Tool software	Sigma	https://www.sigmaaldrich.com/US/en/product/sigma/duo90806?gclid=CjwKCAiA3aeqBhBzEiwAxFiOBqF9uuMdu2hHNnxVEwQGnRC6IqX7PBi1QgpEAjAZVF1akig6ixshsRoCCm0QAvD_BwE

RESOURCE AVAILABILITY

Lead contact

Further information and requests for resources and reagents should be directed to and will be fulfilled by the lead contact, Besim Ogretmen (ogretmen@musc.edu).

Materials availability

All stable reagents generated in this study are available from the lead contact with a completed Materials Transfer Agreement.

Data and code availability

- Original, uncropped western blot image files have been deposited at Mendeley Data, and they are available at: https://doi.org/10.17632/f9wgj84d7z.1.

- Original RNA sequencing files have been deposited and available in: GEO: GSE267312, GSE250637, GSE250638.
- Original proteomics data have been deposited and are available in PRIDE: PXD053108.
- This paper does not report the original code.
- Any additional information required to reanalyze the data reported in this paper is available from the lead contact upon request.

EXPERIMENTAL MODEL AND SUBJECT DETAILS

Animals

Six-to eight-week-old female C57BL/6 mice, Balb/c or FVB mice were purchased from the Jackson Laboratory and used in this study. The animal procedures described below were performed in strict accordance with the Guide for the Care and the Use of Laboratory Animals of the National Institutes of Health. All animals were handled according to the approved Institutional Animal Care and Use Committee (IACUC) protocol at the Medical University of South Carolina and conducted following accepted veterinary and regulatory standards.

4T1 orthotopic model and metastasis analysis

4T1 cells stably expressing SCR or CerS4 shRNA were injected into the mammary fat pads ($1x10^5$ cells in 100 μL of a 50:50 PBS/Geltrex solution) of female BALB/c mice.[1] On day 7, post-injection, the mice began treatment for 21 days. On day 28, the primary tumors and lungs were collected. The lungs were processed and sectioned for downstream analysis using FFPE. Three lung sections per mouse spanning the width of the tissue were H&E stained and submitted to the translational science laboratory core facility at MUSC for analysis.

H&E-stained slides were imaged using the PhenoImager HT Automated Quantitative Pathology Imaging System (Akoya Biosciences, Marlborough, MA) and analyzed using inForm Tissue Analysis Software (v[2.6.0], Akoya Biosciences, Marlborough, MA). Spatial analysis was performed using the PhenoptrReports Open-Source R Package (Akoya Biosciences, Marlborough, MA). The three lung sections for each mouse were averaged before statistical analysis between groups. The Institutional Animal Care and Use Committee (IACUC) at the Medical University of South Carolina approved the protocols used in this study.

MMTV-PyMT metastatic mammary tumor model

Male hemizygous for Tg (MMTV-PyVT) 634Mul mouse (MMTV-PyMT) was purchased from Jackson Lab (022974) and crossed with wild-type (WT) female FVB mice (Jackson, 001800) at 6 weeks of age. Genotyping was done from the tail biopsy of the pups at 3 weeks of age. A female hemizygous MMTV-PyMT mouse with metastatic tumors was sacrificed at 12 weeks of age. Tumors were collected, cut into small pieces of 2 × 2 mm diameter, and transplanted near the 4^{th} mammary fat pad of a cohort of 6-week-old female WT FVB mice. After the average tumor volume reached 90–100 mm^3, mice were equally distributed to treatment groups with similar mean and median across different groups. Treatments were done for 4 weeks. The tumor volume was measured twice weekly, and body weight was measured weekly. Tumor volume was calculated using the formula (length × $width^2$)/2. After 4 weeks of treatment, all mice were sacrificed, and the tumors and spleen were collected and stored for subsequent analysis.

Generation of MMTV-PyMT/CerS4$^{-/-}$ mice and analysis of lung metastasis

MMTV-PyMT (strain B6.FVB-Tg(MMTV-PyVT)634Mul/LellJ) mice were obtained from Jackson Laboratory. CerS4$^{+/-}$ (C57Bl/6) mice were crossbred with MMTV-PyMT mice to generate MMTV-PyMT/CerS4$^{+/-}$ and MMTV-PyMT/CerS4$^{-/-}$ mice. Female MMTV-PyMT/CerS4$^{+/+}$, MMTV-PyMT/CerS4$^{+/-}$, and MMTV-PyMT/CerS4$^{-/-}$ mice progressively developed breast tumors, and specimens were collected 150 days after birth. Primary breast and metastatic lung tumors were measured and quantified by an independent pathologist at the Hollings Cancer Center's Tissue Biorepository Core facility.

Cell lines and culture conditions

4T1, MDA-MB-231, and LM2-4175 cell lines were maintained in DMEM, supplemented with 10% fetal bovine serum, 1% penicillin-streptomycin (100x), and prophylactic plasmocin (InvivoGen). Doxycycline inducible CerS4 LM2-4175 cells were maintained in tetracycline-free fetal bovine serum. Shh signaling was activated using recombinant mouse shh ligand at a dose of 200 μg/mL (Lifespan Bioscience Inc). Stimulation of PD-L1 expression was performed using recombinant mouse IFN-γ at a dose of 100 ng/mL (R&D Systems). Inhibition of TGFBR1, SMO, and Wnt/B-Catenin was performed with Ly2157299 (10 μM), pSMO antibody (2 μg/mL), sonidegib (20 μM), E7386 (1 μM), and tegatrabetan (0.1 μM), respectively. Inhibition of clathrin endocytosis was accomplished with PitStop2 (30 μM for 1 h or 5 μM for 24 h). Inhibition of transcription was accomplished with actinomycin D (5 μg/mL for the specified time).

METHOD DETAILS

Plasmids and antibodies

Lentiviral partials containing lentiviral constructs (obtained from Millipore-Sigma or VectorBuilder) transfected cells for 48 h before antibiotic selection. Antibiotic selection for 4T1 cells was 4 μg/mL Puromycin and 400 μg/mL Hygromycin, while LM2-4175 cells were 6 μg/mL Puromycin and 1000 μg/mL Hygromycin. Lentiviral particles were generated using psPAX2 and pMD2.G plasmids

packaging plasmids, and Effectene (Qiagen) on HEK-293T cells for 72 h, collecting the lentiviral particles on day 2 and day 3. Transient overexpression was obtained by following Effectene (Qiagen) manufacturer protocols and utilizing cells for assays after 48 h. All overexpression and inducible plasmid constructs were purchased from VectorBuilder, where quality control was performed. A list of the plasmids used includes pLV-EV, pLV-PD-L1-WT-FLAG, pLV-PD-L1-Mut-FLAG, pLV-tTS/rtTA, pLV-TRE-CerS4. Scrambled (SCR) shRNAs (non-targeting controls) were obtained from Sigma or VectorBuilder. The specific shRNA constructs are listed below.

CerS4 shRNA: 5′-ATGAATCTCTCAAAGGCAAGG-3′.
Shh shRNA: 5′-ATATGTGCCTTGGACTCGTAG-3′.
SMO shRNA: 5′-AACTGAGATGTGAATGTAGGG-3′.
SCR shRNA: 5′-CCTAAGGTTAAGTCGCCCTCG-3′.
Caprin-1 shRNA: 5′- TCAGTACCAGGCCACTTATAA-3′.
PD-L1 shRNA: 5′-CCGGGCGTTGAAGATACAAGCTCAACTCGAGTTGAGCTTGTATCT TCAACGCTTTTTG-3′.

The antibodies used in this study were as follows: Shh (Cat# sc-365112 Santa Cruz), SMO (Cat# PA5-72395 Invitrogen), Actin (Cat# A2066 Sigma), PTCH1 (Cat# sc-518044 Santa Cruz), CerS4 (Cat# sc-376497 Santa Cruz), CypB (Cat# 43603 Cell Signaling Technology), caprin-1 (Cat# 15112-1-AP, 66352-1-Ig Proteintech), PD-L1 (Cat# ab213480 Abcam, Cat# 124308 Biolegend, Cat# sc-518027 Santa Cruz, Cat# 66248-1-Ig Proteintech, Cat# 329706 Biolegend), ATP1A1 (cat# ab76020 Abcam), TGFBR1 (cat# ab31013 Abcam), FLAG (Cat# F1804 Millipore-Sigma), EXOSC10 (Cat# 11178-1-AP Proteintech), CD3 (Cat# A0452 Agilent), CD8a (Cat# ab217344 Abcam), FoxP3 (Cat# 12653 CST), CD86 (Cat# 19589 Cell Signaling Technology), PanCK (Cat# 760–2595 Roche), Wnt5b (Cat# A8313 Abclonal), TCF7L2 (Cat# 2569 Cell Signaling Technology), Gli1 (Cat# sc-515751 Santa Cruz), Clathrin heavy chain (Cat# MA1-065 Invitrogen), E-cadherin (Cat# 3195 Cell Signaling Technology), PABP (Cat# sc-32318 Santa Cruz), and normal rabbit IgG (Cat# 12–370 Millipore-Sigma).

Cellular migration assay and analysis

Cell migration was measured using Boyden chambers. For migration assays, cells were plated (150,000–250,000 cells per well, depending on the assay and cell line) on a 6-well plate in triplicate. Cells were incubated with or without their respective treatments in serum-free media for at least 24 h. Cells were washed twice with 1x PBS, lifted from the plate with 0.25% trypsin, diluted in fresh serum-free media, and counted for the assay. The inserts for 24-well plates (transparent PET membrane, 4–8.0 μm pore size, Falcon) were pre-coated with Fibronectin (Millipore-Sigma) for 1 h at 37°C. The upper chamber had an assay and cell-line dependent number of cells loaded in serum-free media first, which rested for 10 min at 37°C in a humidified atmosphere with 5% CO2. Any treatments were included in the top chamber during the migration process. After 10 min, complete media (10% serum) was added to the bottom chamber. The volume in the bottom chamber (~600 μL) was adjusted proportionally to the volume in the top chamber (~100 μL) using a 6:1 ratio, respectively. After a 24-h incubation at 37°C humidified atmosphere with 5% CO2, cells were fixed in 4% PFA for 15 min and stained with 0.2% crystal violet for 15 min. Bright-field images were taken with 10x objectives using an Olympus CKX41 or a Zeiss AX10 phase-contrast microscope. Several images (n = 4–6) of the membrane in different regions were taken, and the number of cells per field was averaged for each biological replicate using ImageJ software. The average number of cells migrated for each assay was then normalized to the control. All cell migrations are adjusted for differences in cell proliferation and accurate cell loading according to a proliferation assay running in parallel.

Measurement of ceramides by LC/MS/MS

Cells were collected and washed twice with cold PBS. Further preparation of samples and measurement of endogenous ceramides by LC-MS/MS followed the protocol described previously.[34,69] Briefly, samples were supplemented with internal standards, and 2mL of isopropyl alcohol: water: ethyl acetate (30:10:60; v/v:v) was added to the extracts. Samples were subjected to two rounds of vortex and sonication followed by 10-min centrifugation at 4,000 rpm. The supernatant or top layer was used as lipid extract and subjected to LC-MS/MS for analysis of sphingolipid species. The MUSC Lipidomics Shared Resources performed lipid extraction and analyses. Inorganic phosphates (Pi) or total protein amounts were used for normalization.

Immunofluorescence and immunohistochemistry

For confocal microscopy imaging, Cells were plated (25,000–50,000 cells per well depending on the assay and cell line) on poly-L-lysine coated 35-mm glass-bottomed dishes (MatTek Corporation) or Chamber Slides and incubated in their respective conditions, then washed two times with 1xPBS. Cells were fixed and permeabilized using 4% paraformaldehyde (15 min) and 0.1% Triton X-100 in 1xPBS for 15 min each. The cells were then blocked with 3% BSA in PBS for 1 h at room temperature. Cells were incubated in a humidified chamber for 18 h at 4°C with antibodies specific to PD-L1, CLTC, E-cadherin, or PABP (1:100) and caprin-1 (1:200) in fresh blocking solution, followed by AlexaFluor 488- or 594-conjugated secondary antibodies (1:500) in fresh blocking solution for an additional hour at room temperature. Stained samples were covered using Vectashield HardSet antifade mounting media with DAPI (Vector) and imaged using the Olympus FV10i confocal microscope in channels to visualize AF488, AF594, and DAPI—at least three random image fields selected for each replicate. Images were processed and analyzed using Olympus FluoView Software. Colocalization analysis was performed using ImageJ software.

Proximity ligand assay (PLA) studies

Cells were fixed and permeabilized using 4% paraformaldehyde (15 min) and 0.1% Triton X-100 in 1xPBS for 15min each. Cells were blocked and washed following the Duolink *in situ* hybridization kit manufacturer's instructions and reagents (Olink Biosciences). Cells were incubated in a humidified chamber for 18 h at 4°C with primary antibodies specific to PD-L1, Shh, or PTCH1 (1:100) and caprin-1 (1:200) in antibody dilutant. The remainder of the procedure followed the manufacturer's instructions.

For FFPE samples, slides were baked for 1 h at 60°C, deparaffinized, and rehydrated through a series of xylene and ethanol washes for paraffin-embedded tissues. Heat-induced epitope retrieval was performed for 30 min at 95°C in 1x TRIS-EDTA unmasking solution (Vector). The remainder of the procedure followed the instructions listed above for cells and the manufacturer's instructions. Quantitative output (signals per cell) was normalized to the control for each experiment.

Immunoblotting

Cells and tumor tissues were homogenized in ice-cold Pierce IP lysis buffer (Thermo), including protease inhibitor and phosphatase inhibitor cocktails, and they were allowed to incubate on ice for 30 min. The samples were centrifuged at 12,000 g for 15 min at 4°C. The supernatants were collected, and proteins were quantified by the Pierce 660nm assay (Thermo) method. Loading dye (6x with BME) was added to the appropriate volume of sample and boiled using a heating block at 95°C for 10 min before loading the samples on an SDS gradient gel 4%–20% and running them using the Bio-Rad Criterion apparatus, followed by semi-dry transfer onto PVDF membranes. Blocking was done with 5% bovine serum albumin (BSA) in PBS and 0.1% tween 20 (PBST). Diluted in blocking buffer, primary antibodies were allowed to incubate overnight at 4 °C at the concentration listed below. Horseradish peroxidase (HRP)-conjugated secondary antibodies against mouse or rabbit IgG were added to the membranes in 5% milk in PBST (1:10,000 dilution) for 1 h at room temperature. Enhanced chemiluminescent (ECL) horseradish HRP substrate was then added to the membranes to visualize the proteins of interest using the ChemiDoc imaging system. Proteins of interest included Cers4 (1:400), Shh (1:200), CypB (1:2000), TGFBR1 (1:500), PD-L1 (1:1000), ATP1A1 (1:1000), caprin-1 (1:2000), EXOSC10 (1:1000), SMO (1:1000), Actin (1:5000), FLAG (1:1000), Gli1 (1:1000), TCF7L2 (1:2000), and Wnt5b (1:500).

Immunoprecipitation

Cells were lysed like the standard immunoblotting protocol. Lysates were incubated overnight with corresponding antibodies at 4°C using a 1:100 (μg:μg) ratio, followed by a 1 h incubation with 50 μL washed Pierce Protein A/G Magnetic Beads at 4°C. The resin was washed three times with cold 0.1% PBST, and then pulled-down proteins were analyzed by SDS-PAGE. Gels were transferred onto western blots as described before and probed with antibodies of interest, or gel bands of interest were collected and shipped for proteomic analysis by LC/MS/MS at the Taplin Mass Spectrometry Facility (Harvard University).

Quantitative PCR

Total RNA isolation from cells and tumor tissue was performed using RNeasy (Qiagen), and 500ng of total RNA was used for complementary DNA (cDNA) synthesis using the iScript cDNA Synthesis Kit (Bio-Rad). qPCR probes for different RNAs of interest were prepared, and qPCR was performed using SsoAdvanced universal probes supermix (BioRad). All qPCR used FAM-MGB TaqMan 20x probes purchased from Sigma. Actin or RPLPO was used as the housekeeping reference. The specific qPCR probes are listed in the key resources table.

RNA-immunoprecipitation coupled RT-qPCR

Following the protocol described for general immunoprecipitation with the addition of Protector RNase inhibitor (Roche) to the cell lysis buffer, all subsequent IP steps followed the manufacturer's recommendations. After immunoprecipitation, RNA was isolated using Qiazol (Qiagen) and processed per the manufacturer's instructions. Glycoblue (Thermo Fisher) was used according to manufacturer guidelines to aid RNA isolation. Isolated RNA was handled using the same protocol as previously described in the quantitative PCR section above.

RNA-immunoprecipitation sequencing

Isolated RNA from the RNA-IP was provided to the Translational Science Laboratory Core at MUSC, which performed the sample quality control, RNA library preparation (standard Illumina protocols), and RNA seq analysis. In brief, genes were identified from the RIP seq that were enriched in the pulldown compared to the IgG control and >3-fold more abundant in the group either stably expressing CerS4 shRNA compared to shSCR or in the groups treated with doxycycline compared to the untreated group. From these genes, pathway over-representation was performed to identify pathways differentially influenced using the PANTHER database. Pathways that had more individual genes than anticipated, according to the over-enrichment test, were considered enriched.

Whole-transcriptome sequencing (RNA-seq)

Ribosomal (r)RNA-depleted stranded libraries for each condition (four biological replicates (different tumors) for each vehicle, sonidegib, PD-L1, and combination tumors) were generated and multiplexed. Paired-end 100 bp sequencing was performed using the Illumina HiSeq 2000 platform at McGill University and Genome Quebec Innovation Center. In all, 60–70 million sequencing reads were obtained for each sample. Raw sequence reads were aligned using Gencode vM23 mouse genome annotation and Gencode

Grcm38.p6 mouse reference genome using TopHat with default parameters. *Cufflinks* were used to assemble and quantify transcripts from the mapped sequences.

mRNA stability assays

For mRNA stability assays, cells were plated (150,000–250,000 cells per well, depending on the assay and cell line) on a 6-well plate in triplicate and incubated in their respective conditions, then washed two times with 1x PBS. Fresh complete media was added with or without actinomycin D (5 μg/mL) for the specified time. Samples were collected for downstream RT-qPCR analysis of genes of interest by quickly washing the cells with 1x PBS and proceeding to the RNeasy (Qiagen) protocol. An internal reference control for each group was used to calculate relative mRNA decay by measuring the expression of the genes of interest (Shh and TGFBR1) and housekeeping genes (Actin and RPLPO) at baseline.

Protein sequence analysis by LC-MS/MS

Proteomics analysis was performed in Taplin Biological Mass Spectrometry Facility (Harvard University). Excised gel bands were cut into approximately 1 mm^3 pieces. Gel pieces were then subjected to a modified in-gel trypsin digestion procedure. Gel pieces were washed and dehydrated with acetonitrile for 10 min followed by removal of acetonitrile. Pieces were then completely dried in a speed-vac. Rehydration of the gel pieces was with 50 mM ammonium bicarbonate solution containing 12.5 ng/μL modified sequencing-grade trypsin (Promega, Madison, WI) at 4°C. After 45 min, the excess trypsin solution was removed and replaced with 50 mM ammonium bicarbonate solution to just cover the gel pieces. Samples were then placed in a 37°C for 18 h. Peptides were later extracted by removing the ammonium bicarbonate solution, followed by one wash with a solution containing 50% acetonitrile and 1% formic acid. The extracts were then dried in a speed-vac (~1 h). The samples were then stored at 4°C until analysis.

On the day of analysis, the samples were reconstituted in 5–10 μL of HPLC solvent A (2.5% acetonitrile, 0.1% formic acid). A nano-scale reverse-phase HPLC capillary column was created by packing 2.6 μm C18 spherical silica beads into a fused silica capillary (100 μm inner diameter x ~30 cm length) with a flame-drawn tip. After equilibrating the column each sample was loaded via a Famos auto sampler (LC Packings, San Francisco CA) onto the column. A gradient was formed, and peptides were eluted with increasing concentrations of solvent B (97.5% acetonitrile, 0.1% formic acid). Eluted peptides were subjected to electrospray ionization and then entered in a Velos Orbitrap Pro ion-trap mass spectrometer (Thermo Fisher Scientific, Waltham, MA). Peptides were detected, isolated, and fragmented to produce a tandem mass spectrum of specific fragment ions for each peptide. Peptide sequences (and hence protein identity) were determined by matching protein databases with the acquired fragmentation pattern by the software program, Sequest (Thermo Fisher Scientific, Waltham, MA). All databases include a reversed version of all the sequences. The data was filtered between 1 and 2% peptide false discovery rate.

Isolation and activation of tumor-infiltrating lymphocytes (TILs)

To obtain tumor-infiltrating T cells (TILs) from 4T1-derived tumors, the tumors were carefully excised, chopped finely using tweezers and scissors, and then dissociated using the Miltenyi tumor dissociation kit following protocol mTDK2 and manufacturer instructions. Following dissociation, tumors were filtered through 70 mM cell strainers. The cell suspension was washed in 10 mL of cold DMEM twice and pelleted by centrifugation at 1,500 rpm for 5 min. The pellet was then incubated with 1x ACK lysis buffer (Biolegend) for 1 min at room temperature. After RBC lysis, the sample was diluted with 20 mL 1x PBS and centrifugated at 1500 rpm for 5 min. Next, the cells were resuspended in 4 mL PBS and layered carefully over 4mL Ficoll-paque (Cytiva), followed by centrifugation at 1500 rpm for 30 min. The enriched TILs were obtained by collecting the PBS/Ficoll interface as a thin buffy coat layer and washing with PBS twice and finally in complete media (DMEM media supplemented with 10% FBS, 100 U/ml penicillin, 100 mg/mL streptomycin, 55 mM beta-mercaptoethanol). Purified TILs ($1x10^6$ cells/mL) were activated using anti-CD3 (2μg/ml) and anti-CD28 (5μg/ml) antibodies in the presence of 100 IU/mL IL-2. Cells were incubated in a humidified incubator for 24 h in 5% CO2 atmospheric oxygen at 37°C. To evaluate intracellular cytokines by flow cytometry, a Golgi inhibitor (BD Biosciences) was added according to manufacturer recommendations to the TILs 3 h before staining.

Treatment with anti-PD-L1 and sonidegib *in vivo*

The vehicle group received daily oral gavages (100 μL) of corn oil and twice weekly intraperitoneal injections (100 μL) of 5 mg/kg IgG. The sonidegib group received daily oral gavages (100 μL) of 20 mg/kg sonidegib in a 98% corn oil and 2% DMSO solution. The anti-PD-L1 group received twice weekly intraperitoneal injections (100 μL) of 5 mg/kg anti-PD-L1. The combination group received daily oral gavages (100 μL) of 20 mg/kg sonidegib in a 98% corn oil and 2% DMSO solution and twice weekly intraperitoneal injections (100 μL) of 5 mg/kg PD-L1.

QUANTIFICATION AND STATISTICAL ANALYSIS

Multiplex staining and scanning

Optimized multiplex immunofluorescence was performed using the OPAL multiplexing method. OPAL is based on Tyramide Signal Amplification (TSA) using the Roche Ventana Discovery Ultra Automated Research Stainer (Roche Diagnostics, Indianapolis, IN). Tissues were stained with antibodies against CD3 (1:100), CD8 (1:500), FoxP3 (1:100), CD86 (1:100), PanCK (RTU), Shh (1:50), and

TGFBR1 (1:50) and the fluorescence signals were generated using the different OPAL fluorophores: 480 (1:100), 520 (1:100), 570 (1:50), 620 (1:50), 690 (1:50), and 780 (1:6.25) (Akoya Biosciences, Marlborough, MA). Multiplex-stained slides were imaged using the PhenoImager HT Automated Quantitative Pathology Imaging System (Akoya Biosciences, Marlborough, MA) and analyzed using inForm Tissue Analysis Software (v[2.6.0], Akoya Biosciences, Marlborough, MA). Spatial analysis was performed using the PhenoptrReports Open Source R Package (https://akoyabio.github.io/phenoptrReports/index.html, Akoya Biosciences, Marlborough, MA).

Flow cytometry staining and analysis

Tumor cells were incubated in cell dissociation buffer (Gibco) for 10 min at 37°C and washed once in cold 1x PBS before dilution into FACS buffer (1% BSA, 0.05% Sodium Azide in PBS). Tumor samples were prepared using the TILs isolation protocol, but after incubation with 1x ACK lysis buffer, samples were collected and diluted into FACs buffer. All samples were incubated with FC block (Biolegend) at the recommended dilution for 20 min at 4°C in the dark. Staining for cell surface markers (CD45, CD4, CD8, PD1, LAG3, TIM3, CD25, CD11b, Ly6c, Ly6g, PD-L1, F4/80, TGFBR1, SMO) was performed by incubating cells with the antibody at manufacturer recommended dilutions in FACS buffer for 20 min at 4°C in the dark. For intracellular markers/cytokines (FoxP3, IFNγ, IL10, GZB, TNFα) staining, surface markers were stained before fixation/permeabilization (BD Cytofix/Cytoperm Kit, BD Biosciences). Cells were then incubated with the antibodies for 30 min at 4°C in the dark. Living cells were identified using LIVE/DEAD fixable blue dead cell stain Kit (Invitrogen) which irreversibly binds intracellular free amines exposed in cells with compromised cell membranes. Samples were acquired on LSR Fortessa or Cytek Northern Lights Spectral Analyzer and analyzed with FlowJo software (Tree Star, OR). The general gating strategies are described in Figure S2B. Tumor cells: Total cells → living cells → singlets → marker of interest (i.e., PD-L1). Whole tumor: Total cells → living cells → singlets → $CD45^+$ → CD11b+ (myeloid subpopulations), or CD4/8+ (lymphocyte subpopulations). CD11b+ → F4/80+ or Ly6C/Ly6G+. $CD4^+$ → CD25+FoxP3+ or PD1+ → LAG3+TIM3+. $CD8^+$ → PD1+ → LAG3+TIM3+. TILs: Total cells → living cells → singlets → $CD45^+$ → CD4/8+ → marker of interest (i.e., IL-10).

Statistical analyses

All data are presented as means ± SD (Standard Deviation) of at least three independent studies ($n \geq 3$) unless otherwise noted in the figure legends. Using Graph Pad Prism, group comparisons were performed with either two-tailed unpaired t-tests (and nonparametric tests), one-way ANOVA (and nonparametric or mixed), or two-way ANOVA (and nonparametric or mixed). $p < 0.05$ (*) was considered significant. For comparing survival graphs, the significance was calculated by the Log rank test. Pearson correlation coefficients were calculated using GraphPad Prism Software, 10.1.1, for correlation analysis.

Patient data analyses

Gene expression data from breast cancer patients (GSE25066, GSE58812, and GSE21653) were downloaded using the GEO database (https://www.ncbi.nlm.nih.gov/geo/). For KM-Plotter analysis (https://kmplot.com/analysis/), the auto-select best cut-off option was utilized. To stratify PD-L1 positive and negative individuals in GSE58812, patients were sorted based on PD-L1 mRNA expression and separated from the median. Shh score in patients from GSE58812 was generated by extracting the gene expression data of the genes listed in KEGG's Hedgehog Signaling Pathway. Gene expression data were then converted to z-scores using SPSS software, and the sum of the z-scores of the genes in the list was assigned as the Shh score for each patient. Separations of patients based on Cers4, CTNNB1, Wnt5b, TCF7L2, and Shh score levels were performed using median expression. Finally, Kaplan Meier survival analyses were performed using specific patient sub-populations indicated in legends by grouping patients based on the individual or combined expressions of CerS4, CTNNB1, Wnt5b, and TCF7L2 mRNA, as shown in figure legends.